

REPORT

CRYSTAL GROWTH

Controlled growth and form of precipitating microsculptures

C. Nadir Kaplan,^{1,2*} Wim L. Noorduyn,^{1,3*} Ling Li,^{1,4,5} Roel Sadza,¹ Laura Folkertsma,¹ Joanna Aizenberg,^{1,2,4,6} L. Mahadevan^{1,2,4,7,†}

Controlled self-assembly of three-dimensional shapes holds great potential for fabrication of functional materials. Their practical realization requires a theoretical framework to quantify and guide the dynamic sculpting of the curved structures that often arise in accretive mineralization. Motivated by a variety of bioinspired coprecipitation patterns of carbonate and silica, we develop a geometrical theory for the kinetics of the growth front that leaves behind thin-walled complex structures. Our theory explains the range of previously observed experimental patterns and, in addition, predicts unexplored assembly pathways. This allows us to design a number of functional base shapes of optical microstructures, which we synthesize to demonstrate their light-guiding capabilities. Overall, our framework provides a way to understand and control the growth and form of functional precipitating microsculptures.

Microstructures with complex three-dimensional (3D) shapes emerge as important elements in magnetic, electronic, and optical devices (1–4). Well-defined highly curved and hollow shapes are increasingly essential for sophisticated microphotonic components, such as optical resonance cavities (5–7), light directors (8), photonic trumpets (9), and next-generation optical metamaterials (4, 10, 11). Currently, none of the existing fabrication approaches takes full advantage of the physicochemical processes that arise in natural systems. Top-down lithographic manufacturing has the capability of creating complex 3D geometries precisely but is laborious and difficult to scale up. Similarly, molding and 3D printing show enormous potential in building intricate shapes but have limited ability to control feature sizes at the submicron scale (12, 13). Finally, droplet microfluidics or colloidal self-assembly are simple and scalable but typically form highly symmetric superstructures (14, 15).

A promising candidate for the bottom-up fabrication of cheap, scalable, and intricate geometries is the biomineralization-inspired coprecipitation of silica with barium or strontium carbonates (16–22). The resulting structures—such as vases, corals, and helices (Fig. 1, A to D)—can be rationally sculpted by modulating the reaction conditions

(22). Although semiempirical arguments allow for a qualitative view of the mechanisms involved, the absence of a quantitative theoretical framework makes it difficult to characterize or control these precipitation patterns. Here, we provide a geometrical theory for the morphogenesis of carbonate-silica coprecipitation as an interface growth problem. We use the theory to explore the range of possible shapes and determine ways to control them.

When CO₂ flows into an alkaline aqueous solution (pH = 11 to 12) of barium chloride (BaCl₂) and sodium metasilicate (Na₂SiO₃), carbonate-silica structures coprecipitate in three stages (Fig. 1E) [section I. A in the supplementary materials (SM)]: (i) Barium carbonate (BaCO₃) crystallizes in the entire basic pH range according to Ba²⁺ + CO₂ + H₂O → BaCO₃(s) + 2H⁺ (Fig. 1F); (ii) the local decrease in the pH triggers the acid-catalyzed reaction of silicate to orthosilicic acid [Si(OH)₄] in a narrow pH range (Fig. 1F and Eq. S2) and its polycondensation into amorphous SiO₂ on the dendritic BaCO₃ crystals (23), leading to cylindrical posts; and (iii) abundant CO₂ dissolved in the solution induces splitting of the growing tips into either a single connected front at high nucleation densities or multiple disconnected fronts at low nucleation densities, both of which form thin walls composed of rod-shaped BaCO₃ nanocrystals coated by SiO₂ on the lateral wall faces (section II. A in the SM) (20, 22). Because BaCO₃ is produced at higher rates than SiO₂ (section II. A in the SM), the pH at the growth site is lower than that in the bulk solution. Note that when the local pH is within the SiO₂ deposition range, silica precipitates and terminates the growth of BaCO₃ crystals. Therefore, successful carbonate-silica coprecipitation only occurs when the local pH at the growth front is either slightly above (regime I) or below (regime II) the SiO₂ deposition range, so as to sustain con-

tinuous carbonate precipitation (22) (Fig. 1F; section II. A in the SM).

In regime I, the pH of the solution is set significantly higher (pH ≈ 12) than that associated with SiO₂ deposition, resulting in growth directed from the low-pH front toward the high-pH bulk solution where the BaCO₃ supersaturation is higher (Fig. 1F). Consequently, at high nucleation densities, vase-like (Fig. 1A) and petal-like (Fig. 1B) structures grow steeply away from the vicinity of other growing fronts, whereas at low nucleation densities, multiple fronts originating from a single root blossom into coral-like structures (Fig. 1C). We quantified the growth in this regime via a microfluidic reactor that allowed for direct in situ visualization under constant reaction conditions (section I. B to D in the SM and movie S1). When CO₂ enters the microfluidic channel through a membrane, corals nucleate in distinct bands (Fig. 1G) with a spatial and temporal periodicity (section I. E in the SM). Approximating each coral by a hemisphere with a time-dependent radius $R(t)$, we find that the projected circular area of the corals grows linearly in time ($\pi R^2 \cong t$) with a rate of 30 to 50 μm²/min (Fig. 1H). The radius R and the growth speed, U , scale as $R \cong \sqrt{t}$ and $U \equiv dR/dt \cong 1/R$, respectively, i.e., growth is diffusion-controlled at the coprecipitation fronts with a rate proportional to the interfacial curvature, $1/R$ (24, 25). In the vicinity of the front, the soluble silica oligomers may buffer the local acidity and act as slow-diffusing species. The growth of corals reduces the local pH and eventually stops when silica passivates the low-pH fronts that approach each other.

In regime II, the initial bulk solution pH only slightly exceeds that for silica deposition (pH ≈ 11). Carbonate precipitation steers the structures toward each other's growth fronts or close to the substrate, where the local pH at the growth site remains below the pH range of excessive silica formation that would overgrow BaCO₃ crystals and passivate growth (22) (Fig. 1F). This yields helical or leaf-shaped structures (fig. S6C), which develop a high-curvature front that must result in a lower oligomer concentration at the interface (25). The buffering ability of the oligomers is then reduced, which induces the lowering of the local pH. As a result, structures inherently bend away from the bulk with an increased curvature. Helical structures display a high edge-to-surface ratio with strong curling of the walls, both of which reduce the pH at the growth site (Fig. 1D). Leaves grow along the substrate by forming a curved front (fig. S6C), which must again sustain carbonate precipitation by having a localized zone of sufficiently low pH at the growth site. Evolving leaves develop tips with high curvature, where the precipitation rate increases and, in turn, sharpens the tips even more (21). We interpret this as a growth instability characteristic of a diffusion-limited process (25).

In either regime, after front splitting [Fig. 1E, stage (iii)], a diffusion-limited growth front lays down a thin-walled structure. The wall thickness, w , is limited by the SiO₂ precipitation to $w \approx 0.5$ to 0.8 μm even as the wall itself continues to

¹Paulson School of Engineering and Applied Sciences, Harvard University, Cambridge, MA 02138, USA. ²Kavli Institute for Bionano Science and Technology, Harvard University, Cambridge, MA 02138, USA. ³AMOLF, 1098 XG Amsterdam, Netherlands. ⁴Wyss Institute for Biologically Inspired Engineering, Cambridge, MA 02138, USA.

⁵Department of Mechanical Engineering, Virginia Tech, Blacksburg, VA 24061, USA. ⁶Department of Chemistry and Chemical Biology, Harvard University, Cambridge, MA 02138, USA. ⁷Department of Physics, Harvard University, Cambridge, MA 02138, USA.

*These authors contributed equally to this work. †Corresponding author. Email: lmahadev@g.harvard.edu

extend laterally over lengths of order 10 μm or larger (section II. A in the SM). The resulting low-aspect ratio structure may thus be well approximated as a surface that is left behind by a space curve, which represents the growth front and evolves over time (Fig. 2A). The instantaneous configuration of the growth front and its embedding in the surface can be formulated in terms of the curve metric, g ; the geodesic curvature, κ_g ; the normal curvature, κ_N ; the geodesic torsion, τ_g ; and the second normal curvature, $\kappa_{N,2}$ (Fig. 2, B and C, and table S2). The variables κ_g , κ_N , τ_g , and g are linked by the partial differential equations of surface theory in differential geometry (26) that embody the geometric constraints on the curve embedded in a surface (section II. B in the SM). The position of the moving front $\vec{\mathbf{X}}$ is determined by its evolving Lagrangian velocity

$$\frac{d\vec{\mathbf{X}}}{dt} = \hat{\mathbf{n}}U \quad (1)$$

where $\hat{\mathbf{n}}$ is the growth direction, U is the local speed of the curved front, $d/dt \equiv \partial/\partial t|_{\vec{\mathbf{x}}(s,t)}$ (see Fig. 2A). To characterize the diffusion-limited accretion, we assume that U is a function of the local geometry of the growth front, as in dendritic patterning processes (27). Our assumption is justified by the localized growth due to the coprecipitation reactions (Eqs. S1 and S2) and slow diffusion of soluble silica oligomers. This corresponds to the inequality $w \ll L_D < L_\kappa$, where w is the wall thickness, L_D is the diffusion length and L_κ is the radius of curvature. In contrast, growth of a 2D front in dendritic solidification is diffusion-

controlled only when it is nonlocal, i.e., $L_D > L_\kappa$ (section II. C in the SM). Writing $U = U(\kappa_g, \kappa_N, \tau_g, \kappa_{N,2})$ and expanding this function as a power series up to cubic order (section II. D in the SM), the resulting equations of motion for U and the geometrical variables ($g, \kappa_g, \kappa_N, \tau_g, \kappa_{N,2}$) yield the position of the growth front $\vec{\mathbf{X}}$ from Eq. 1, and the surface left behind by it, given the second normal curvature, $\kappa_{N,2}$.

The variable $\kappa_{N,2}$ controls the local bend distortions along the growth direction, $\hat{\mathbf{n}}$, and it is either enhanced or reduced by the initial pH of the bulk solution. This suggests a pH-dependent coarse-grained bending parameter $q_b = q_b(\text{pH})$. In regime I, the growth direction toward the high-pH solution is roughly preserved (Fig. 1, A and B); thus, q_b must be low. In regime II, inward-directed growth toward lower pH forces the structures to curl gradually at the interface (Fig. 1D); therefore, q_b must be high. Experimentally, the bending deformations are governed by the pH gradients at the scale of the wall thickness, w (Fig. 2A). Because we focus on the wall morphogenesis at length scales much bigger than w , we propose the following phenomenological equation of motion for $\kappa_{N,2}$ to characterize both regimes

$$\frac{d\kappa_{N,2}}{dt} = \gamma \frac{\partial^2 \kappa_{N,2}}{\partial s^2} + \zeta \kappa_g \kappa_N U (\kappa_{N,2} - q_b) \quad (2)$$

The first term on the right models the diffusive relaxation of the curling mode along the edge (20) with a diffusivity γ (Fig. 2D). The second term controls bending with a rate ζ by accounting for the following observations: First, bending saturates when $\kappa_{N,2} = q_b$; second, the sign of the geo-

desic curvature, κ_g , determines whether bending should increase or decrease, which allows for dynamic modulations between different growth regimes; third, bending increases more slowly in relatively flat sections with a small normal curvature, κ_N , than in already curled regions with a higher κ_N ; and last, bending stops when the speed U vanishes. Eqs. 1 and 2, and the geometrical compatibility relations (section II. B in the SM), complete the formulation of the problem when initial and boundary conditions are provided.

Given q_b and the angle β that sets the initial orientation of $\hat{\mathbf{n}}$, we simulated the evolution of walls that emerge after front splitting [Fig. 1E, stage (iii)], in particular the vaselike and petal-like structures in regime I and helices in regime II (section II. E in the SM and movies S2 to S6). In Fig. 3A, we show the formation of vases that start from a circle of radius ℓ . To model the experimentally observed correlation between the high nucleation density of precipitates and vase formation, we take the initial growth direction to be strongly out of the substrate plane (β : large, Fig. 1E). As the planar and circular growth site of a vase expands over time, its geodesic curvature, κ_g , decreases (Fig. 2B). When the growth speed U is linear in κ_g , we analytically deduce that the projected area of a vase varies linearly in time (section II. F in the SM). By contrast, growth is sublinear when U also depends on higher-order terms (fig. S8), and the projected area of a vase as a function of time is in accordance with the microfluidics experiments at low q_b (Fig. 1H). Whereas low values of q_b (high pH) lead to cones, for higher q_b (lower pH) the conical vases start to curve

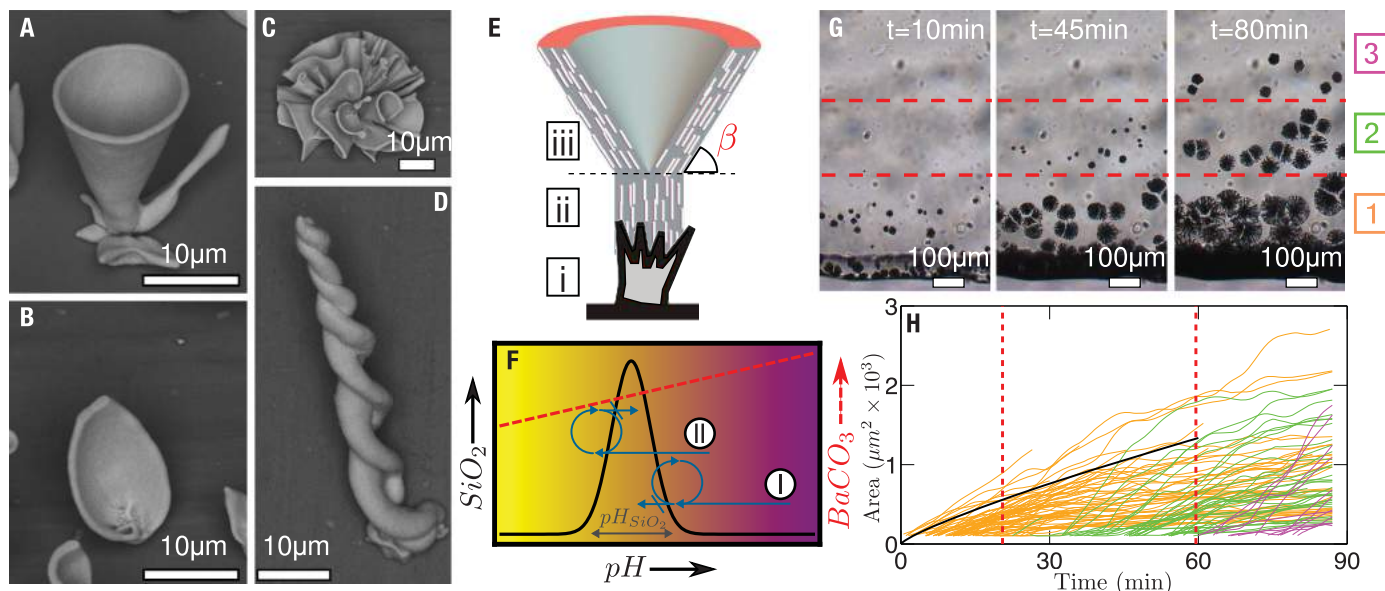


Fig. 1. Carbonate-silica coprecipitation patterns. (A) to (D) Scanning electron microscopy (SEM) images of the typical (A) vasselike, (B) petal-like, (C) coral-like, and (D) helical microstructures. (E) Stages of coprecipitation: (i) nucleation of the seed carbonate crystal; (ii) outgrowth of carbonate/silica coprecipitate; (iii) splitting of the thin wall. The initial slope between a thin wall and the substrate is defined by β . (F) Schematics of the SiO_2 (solid black curve) and BaCO_3 (dashed red line) precipitation rates between pH 8

and 12 (22). Regimes I and II are indicated. (G) Growth of coral-like structures produces three distinct bands (marked alongside with orange, 1; green, 2; and magenta, 3, from bottom to top) in a microfluidic chamber where the CO_2 flows from the bottom edge. (H) Projected circular area of growing corals as a function of time [line colors correspond to the bands in (G)], and the simulated growth of a conical vase for the bending parameter $q_b = 10^{-3}$ (black line, see text).

inwards (Fig. 3A). When the speed of the front is set to zero at a point of the advancing front that starts from a circle, we see nonuniform growth associated with the local passivation by silica overcoating. This leads to the formation of petals

for both low and high q_b as shown in Fig. 3B and fig. S9, respectively, and in agreement with experiments (Fig. 1B).

Finally, helices emerge by means of the unstable growth of a nearly semicircular front as shown in

Fig. 3C. We observe that the pitch and overall size of the helices become larger when q_b decreases (fig. S10), whereas the growth reaches a steady state at lower q_b with a constant pitch and width over the twisted region. At still higher q_b , the helices develop tips and stop (fig. S10), consistent with experiments (20, 22). For an areal growth rate of $40 \mu\text{m}^2/\text{min}$ and an initial radius of $\ell \sim 2 \mu\text{m}$, we see that vases and helices reach a size of $\mathcal{O}(10 \mu\text{m})$ in $\mathcal{O}(10 \text{ min})$, in quantitative agreement with experiments (fig. S8) (see section III. A in the SM for the stereolithography files of the simulated sculptures).

Our theoretical framework couples two physicochemical processes to the instantaneous local geometry of the reaction front and, in turn, the morphology of carbonate-silica precipitates. These processes are the diffusion-limited growth, which is localized by the condition $L_D < L_\kappa$ (where L_D is the diffusion length and L_κ , local radius of curvature) and, hence, quantified by the local growth rate U , and the effect of solution pH on the emergence of curling deformations, modeled by the bending parameter q_b and Eq. 2. The agreement between theoretical and experimental shapes establishes the relation between q_b and pH, as plotted in Fig. 3D.

Photonic microcomponents—such as optical waveguides, light directors (8), and Bragg resonators (7)—are excellent candidates for bottom-up design owing to their shell-like geometries and stringent tolerances. Given the transparency and relatively high refractive index n of the carbonate salts ($n = 1.5$ to 1.7) and silica ($n = 1.5$), the similarity of size and shape between vaselike precipitates (Fig. 3A) and top-down lithographically fabricated analogs (8, 9) suggests the use of our bottom-up strategy to build optical components. To solve the inverse problem of designing functional shapes, we split the simulations into a sequence of steps corresponding to switching growth

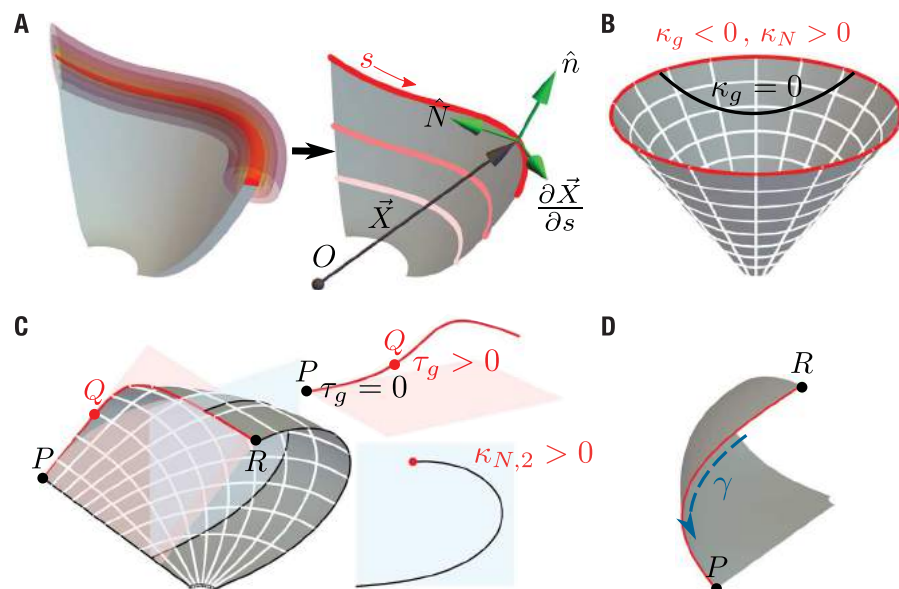


Fig. 2. Geometry of growth. (A) Precipitation in a narrow semicylindrical edge zone leaves behind a thin wall (left). Colors depict the pH values (Fig. 1F). We represent the moving growth front as a curve (shades of red, right) with a position vector, $\vec{X}(s, t)$. An orthonormal triad is formed by the curve tangent, $\partial \vec{X} / \partial s$, the growth direction \hat{n} , both of which lie in the surface, and the surface normal, $\hat{N} = \partial \vec{X} / \partial s \times \hat{n}$. (B) The front geometry is partly determined by the geodesic curvature, κ_g , the curvature of a line with respect to a geodesic ($\kappa_g = 0$) on a surface (26). Folding a plane into the cone introduces a normal curvature (κ_N) along the curve. (C) Unless the orthonormal triad twists, the geodesic torsion, τ_g , characterizes a nonplanar curve; it is zero around the point P where the front is tangent to the light red plane. At point Q , the front becomes a space curve (as τ_g is finite). The second normal curvature, $\kappa_{N,2}$, is associated with the bending of the surface at the front (black curve on the light blue plane). (D) Curling diffuses from high $\kappa_{N,2}$ (at R) to lower $\kappa_{N,2}$ (around P) with diffusivity γ according to Eq. 2.

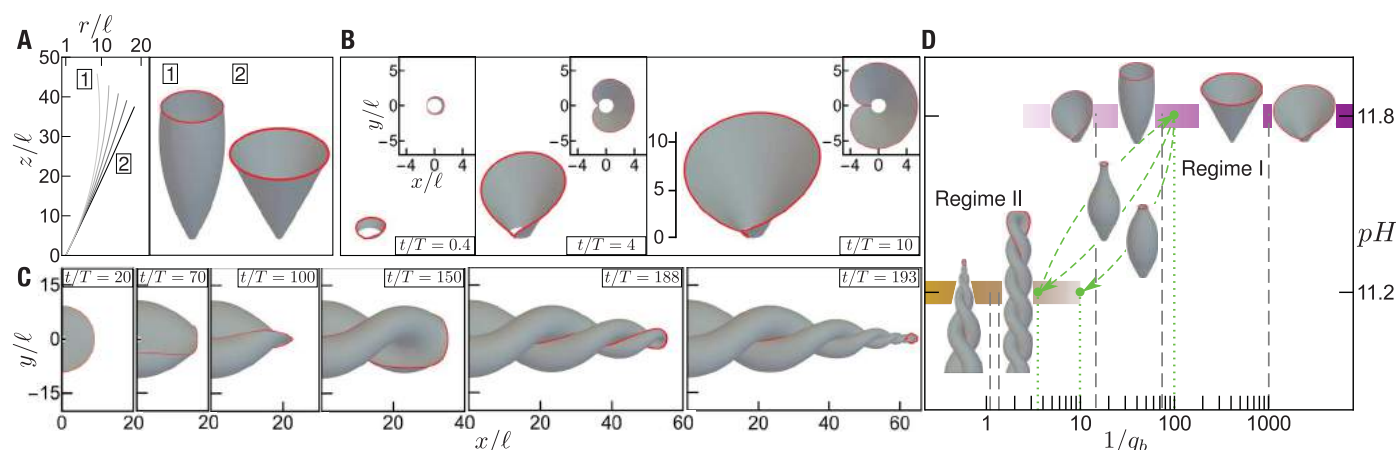


Fig. 3. Dynamics of form. (A) (Left) Axisymmetric profiles of the vases as a function of the bending parameter $q_b \in [10^{-3} - 0.013]$ in 3×10^{-3} increments with the gray scale changing from dark to light. (Right) Resulting vases corresponding to $q_b = 0.013$ (1) and $q_b = 10^{-3}$ (2). (B) Time evolution of petal growth ($q_b = 10^{-3}$), showing the elevated and plan views. (C) Growth of a helical precipitate ($q_b = 0.9$). In (A) to (C), the lengths x , y , z , and r are scaled by ℓ , defined as the radius of the initial circular front, and the

time is scaled by T (see section II. E in the SM). (D) Relation between the reciprocal bending parameter $1/q_b$ and the initial solution pH (regime I pH, magenta; regime II pH, orange) defines the two regimes. The q_b value of each structure is represented by the nearest dashed gray line. The structures grown by the successive modulations between the two regimes (green dashed arrows) correspond to a set of q_b values (green dotted lines) (Fig. 4A).

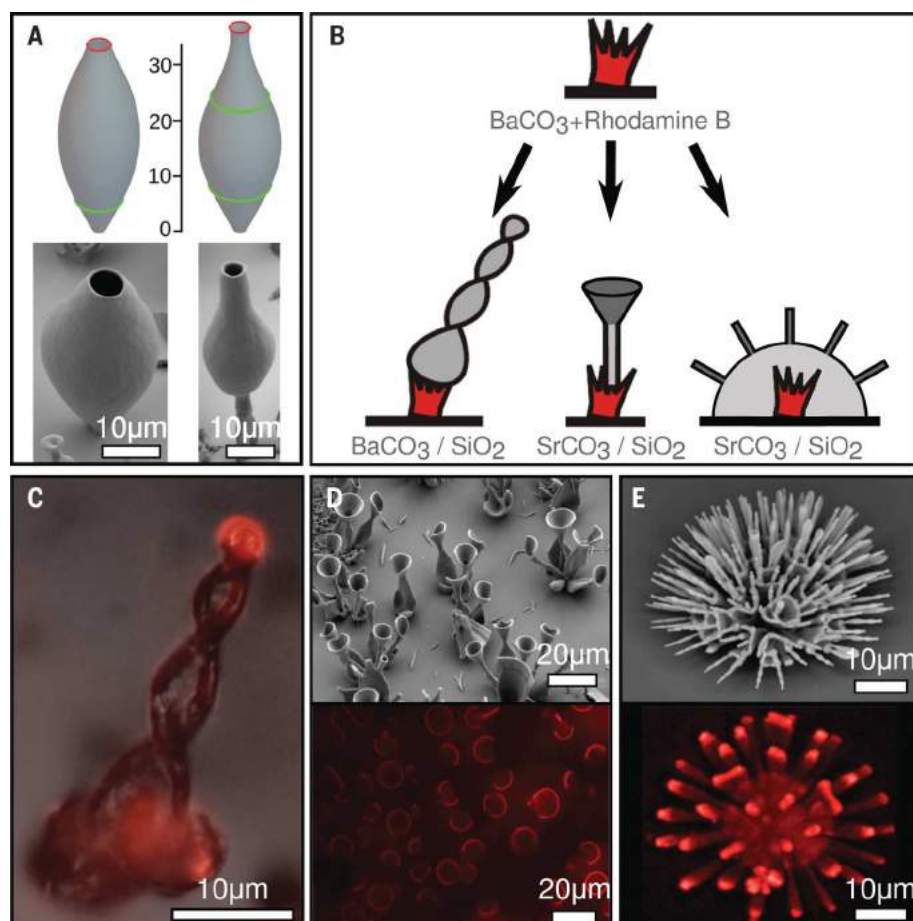


Fig. 4. Controlled growth and form of optical microcomponents. (A) Simulations (top) and experimental realization (bottom) of the base shapes for Bragg resonators. The simulations correspond to the sequences $q_b = 0.01, 0.1$ (top, left) and $q_b = 0.01, 0.3, 0.01$ (top, right). The green curves denote the heights at which q_b changes. The lengths are scaled by ℓ . Likewise, the experimental shapes are grown by two (bottom, left) and three (bottom, right) steps. (B) Schematics for synthesizing microstructures with integrated light source (red) and waveguide properties. The gray scale denotes the growth sequence (section I. G in the SM). (C) Helical structure (overlay of fluorescence and optical microscopy) and (D) trumpet-shaped assemblages (top, SEM image, and bottom, confocal microscopy image) that operate as waveguides. (E) A coral decorated with posts (top, SEM) acting as a beamsplitter (bottom, confocal).

conditions from regime I to regime II, where the final state of the growth site from the preceding step serves as the initial condition for the next regime (movies S7 and S8). For example, our theory predicts that curved precipitates depicted in Fig. 4A (top) may arise in two or three consecutive steps. Starting from a vase with low q_b (high pH), inducing bend at a higher q_b (lower pH) results in the formation of hollow shapes that resemble spherically symmetrical Bragg resonators (5, 6). Reverting to a low q_b (high pH) as a third step plants a narrow neck on top and generates the base shape of an onionlike Bragg resonator similar to that described in (7). This theoretical sequence of alternating growth conditions associated with stepwise changes of q_b in the model corresponds to the control of the pH around a structure (Fig. 3D), indicating how these geometries can also be realized experimentally. These shapes were successfully synthesized following the theoretical guidance (Fig. 4A, bottom, and section I. F in the SM).

To demonstrate that our carbonate-silica precipitates are optically functional, we incorporated a light source in the system. Crystallizing BaCO_3 can be doped with organic additives, including dyes, during precipitation (28). To this end, for the growth stage (i), we introduced the fluorescent dye rhodamine B into the initial solution containing BaCl_2 (section I. G in the SM). The resulting BaCO_3 crystals with the embedded light source served as seeds for subsequent dye-free synthesis of various $\text{BaCO}_3\text{-SiO}_2$ or $\text{SrCO}_3\text{-SiO}_2$ microstructures at the growth stages (ii) and (iii) (Fig. 4B), in which light is effectively directed from the fluorescent crystal to the edge. The thus synthesized helix, photonic trumpets, and an array of posts grown atop a coral, which clearly demonstrate the ability to guide or split light beams, are shown in Fig. 4, C to E.

Our theoretical model explains the range of patterns in a carbonate-silica system and offers a means to guide the synthesis of complex 3D shapes. We have used this bottom-up strategy to

make functional optical microarchitectures using the underlying physicochemical processes in sharp contrast to top-down lithographic methods. When combined with an optimization algorithm for process control, our approach has the potential to provide a scalable, inexpensive, and accurate strategy to create 3D photonic microstructures.

REFERENCES AND NOTES

1. S. Xu et al., *Science* **347**, 154–159 (2015).
2. P. X. Gao et al., *Science* **309**, 1700–1704 (2005).
3. B. M. Ross, L. Y. Wu, L. P. Lee, *Nano Lett.* **11**, 2590–2595 (2011).
4. M. Decker, M. W. Klein, M. Wegener, S. Linden, *Opt. Lett.* **32**, 856–858 (2007).
5. M. A. Kaliteevski, S. Brand, R. A. Abram, V. V. Nikolaev, *J. Mod. Opt.* **48**, 1503–1516 (2001).
6. D. Brady, G. Papen, J. E. Sipe, *J. Opt. Soc. Am. B* **10**, 644 (1993).
7. Y. Xu, W. Liang, A. Yariv, J. G. Fleming, S.-Y. Lin, *Opt. Lett.* **29**, 424–426 (2004).
8. J. H. Atwater et al., *Appl. Phys. Lett.* **99**, 151113 (2011).
9. M. Munsch et al., *Phys. Rev. Lett.* **110**, 177402 (2013).
10. C. M. Soukoulis, S. Linden, M. Wegener, *Science* **315**, 47–49 (2007).
11. J. K. Gansel et al., *Science* **325**, 1513–1515 (2009).
12. J. L. Perry, K. P. Herlihy, M. E. Napier, J. M. Desimone, *Acc. Chem. Res.* **44**, 990–998 (2011).
13. J. R. Tumbleston et al., *Science* **347**, 1349–1352 (2015).
14. S. S. Datta et al., *Adv. Mater.* **26**, 2205–2218 (2014).
15. X. Ye et al., *Proc. Natl. Acad. Sci. U.S.A.* **107**, 22430–22435 (2010).
16. L. A. Gower, D. A. Tirrell, *J. Cryst. Growth* **191**, 153–160 (1998).
17. A. G. Shtukenberg, Y. O. Punin, A. Gujral, B. Kahr, *Angew. Chem. Int. Ed. Engl.* **53**, 672–699 (2014).
18. Y.-Y. Kim et al., *Nat. Mater.* **15**, 903–910 (2016).
19. J. M. García-Ruiz et al., *Science* **302**, 1194–1197 (2003).
20. J. M. García-Ruiz, E. Melero-García, S. T. Hyde, *Science* **323**, 362–365 (2009).
21. M. Kellermeier et al., *Chemistry* **18**, 2272–2282 (2012).
22. W. L. Noorduin, A. Grinthal, L. Mahadevan, J. Aizenberg, *Science* **340**, 832–837 (2013).
23. D. J. Belton, O. Deschaume, C. C. Perry, *FEBS J.* **279**, 1710–1720 (2012).
24. N. Goldenfeld, *J. Cryst. Growth* **84**, 601–608 (1987).
25. J. S. Langer, *Rev. Mod. Phys.* **52**, 1–28 (1980).
26. J. J. Stoker, *Differential Geometry* (Wiley, New York, 1969).
27. R. C. Brower, D. A. Kessler, J. Koplik, H. Levine, *Phys. Rev. Lett.* **51**, 1111–1114 (1983).
28. B. Kahr, R. W. Gurney, *Chem. Rev.* **101**, 893–951 (2001).

ACKNOWLEDGMENTS

The authors thank J. A. Fritz, M. Kolle, M. Lončar, and T. M. Schneider for fruitful discussions and P. A. Korevaar, W. M. van Rees, J. C. Weaver, and T. C. Ferrante for technical assistance. This research was supported by NSF Designing Materials to Revolutionize and Engineer Our Future under award 15-33985, the Kavli Institute for Bionano Science and Technology at Harvard University, and the Harvard MRSEC under award 14-20570. W.L.N. thanks the Netherlands Organization for Scientific Research (NWO) for financial support from a VENI grant. R.S. acknowledges Technical University Eindhoven's Fonds Ectspunten Buitenland financial support, and L.F. the Radboud University Nijmegen study fund. L. M. was partially supported by fellowships from the MacArthur Foundation and the Radcliffe Institute. Scanning and transmission electron microscopies were performed at the Center for Nanoscale Systems at Harvard University, supported by the NSF under award ECS-0335765, and the Amsterdam nanoCenter, supported by NWO. The authors declare no conflicts of interest.

SUPPLEMENTARY MATERIALS

www.sciencemag.org/content/355/6332/1395/suppl/DC1
Materials and Methods
Supplementary Text
Figs. S1 to S10
Tables S1 to S3
Movie Legends S1 to S8
Database Legends S1 to S11
References (29–31)
Movies S1 to S8
Data Files S1 to S11

24 July 2016; resubmitted 31 October 2016
Accepted 9 March 2017
10.1126/science.aah6350



Controlled growth and form of precipitating microsculptures
C. Nadir Kaplan, Wim L. Noorduin, Ling Li, Roel Sadza, Laura Folkertsma, Joanna Aizenberg and L. Mahadevan (March 30, 2017)
Science **355** (6332), 1395-1399. [doi: 10.1126/science.aah6350]

Editor's Summary

Predicting the shape of crystals to come

Coprecipitating carbonate and silica can form complex three-dimensional shapes. These range from flowers to trumpets, depending on the pH. Kaplan *et al.* developed a theoretical model to interpret the crystal growth shapes. The model predicts crystal growth shapes under varying experimental conditions and captures the geometrical aspects of morphological development.

Science, this issue p. 1395

This copy is for your personal, non-commercial use only.

- | | |
|----------------------|--|
| Article Tools | Visit the online version of this article to access the personalization and article tools: http://science.sciencemag.org/content/355/6332/1395 |
| Permissions | Obtain information about reproducing this article: http://www.sciencemag.org/about/permissions.dtl |

Science (print ISSN 0036-8075; online ISSN 1095-9203) is published weekly, except the last week in December, by the American Association for the Advancement of Science, 1200 New York Avenue NW, Washington, DC 20005. Copyright 2016 by the American Association for the Advancement of Science; all rights reserved. The title *Science* is a registered trademark of AAAS.

Supplementary Materials for **Controlled growth and form of precipitating microsculptures**

C. Nadir Kaplan,* Wim L. Noorduyn,* Ling Li, Roel Sadza, Laura Folkertsma, Joanna Aizenberg, L. Mahadevan†

*These authors contributed equally to this work.

†Corresponding author. Email: lm@seas.harvard.edu

Published 31 March 2017, *Science* **355**, 1395 (2017)
DOI: 10.1126/science.aah6350

This PDF file includes

Materials and Methods
Supplementary Text
Figs. S1 to S10
Tables S1 to S3
Movie legends S1 to S8
Database legends S1 to S11
References

Other Supplementary Material for this manuscript includes the following:
(available at www.sciencemag.org/content/355/6332/1395/suppl/DC1)

Movies S1 to S8

Databases S1 to S11 as zipped archives:

- _ vase1 zdim 7.5 cm thickness 2.5mm.zip
- _ vase2 zdim 9.1 cm thickness 2.5mm.zip
- _ petal1 zdim 5.6 cm thickness 2.5mm.zip
- _ petal2 zdim 7.2 cm thickness 2.5mm.zip
- _ helix1 xdim 27.1cm thickness 2.5mm.zip
- _ helix2 xdim 15.3cm thickness 2.0mm.zip
- _ helix3 xdim 9.8cm thickness 2.0mm.zip
- _ pottery 2steps1 zdim 10.1cm thickness 2.5mm.zip
- _ pottery 2steps2 zdim 7.3cm thickness 2.5mm.zip
- _ pottery 3steps1 zdim 10.8cm thickness 2.5mm.zip
- _ pottery 3steps2 zdim 10.9cm thickness 2.5mm.zip

I. Experimental materials and methods

A) Growth of carbonate/silica structures. An aluminum slide was vertically positioned in a 100 mL beaker containing 15 ml aqueous solution of BaCl_2 (19.1 mM) and Na_2SiO_3 (8.2 mM) (Sigma Aldrich). The reaction vessel was loosely covered with a Petri dish to allow CO_2 from the air to diffuse into the system. The pH was measured using a Mettler Toledo FE20 FiveEasy pH meter and adjusted to either 11.9 (Regime I) or 11.2 (Regime II) by adding HCl or NaOH. After 2-3 h, the experiment was stopped by carefully transferring the samples into pure water to terminate the reaction. Subsequently, the samples were placed in acetone for 3 min to replace water with a low surface tension liquid, and carefully dried in the air. Sample analysis was performed using a Leica DMRX optical microscope equipped with polarizers and a FEI Verios 460 scanning electron microscope (SEM) that was equipped with a SE2 detector and a four-quadrant electron backscatter detector.

B) Fabrication of the microfluidic device. A master was made by laser cutting the desired channels out of three layers of double-sided adhesive paper, which was then stuck to a glass slide (see Fig. S1 for the design mold). The typical width of the channels was 1.8 mm, the length 18.6–36.9 mm, the height 150–200 μm , and the thickness of the membrane between the growth channel and the CO_2 channel was 1.1 mm. This master was plasma cleaned and functionalized with a demolding agent (tridecafluoro-1,1,2,2-tetrahydrooctyl)-trichlorosilane (Gelest Inc.) by exposure in a desiccator under vacuum overnight. For polydimethylsiloxane (PDMS) molding of the functionalized master, we used DowSylgard 184 with a prepolymer:curing agent ratio of 10:1. After extensive mixing of the prepolymer and curing agent, the mixture was poured onto the master and placed in a vacuum desiccator for 1 h to eliminate air bubbles. The sample was then thermally cured in an oven for 3 h at 70°C. After cooling, the negative PDMS mold was gently peeled off the master. To insert the tubing into the channels, holes were punched through the PDMS, at both the start and end points of the channels. Tubing was put into these holes and the device was clamped between two glass plates. Syringes containing growth media were

attached to the ends of the tubing and syringe pumps were used to let the solution flow through the channels in a controlled manner.

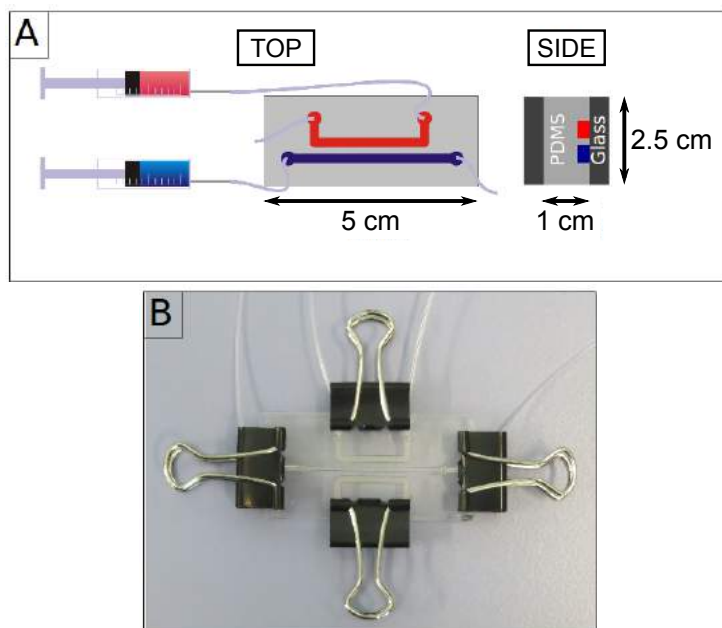


Fig. S1: Microfluidic setup. (A) Schematics of the top and side view of the microfluidic device for the growth of corals that was made by clamping PDMS (light gray) containing the microchannels on top of a glass slide (dark gray). The channel indicated in red contains the NaHCO_3 solution whereas the blue channel is filled with the degassed $\text{BaCl}_2/\text{Na}_2\text{SiO}_3$ solution. The deposition of the $\text{BaCO}_3/\text{SiO}_2$ microstructures is triggered in the blue channel by the influx of CO_2 from the red channel via the thin PDMS wall that separates the two channels. (B) The experimental setup of the microfluidic device. The dimensions of the structure are given in (A). The microfluidic design contains an additional channel to which NaHCO_3 solution can be pumped. This allows us to perform a second experiment simultaneously.

C) Preparation of the solutions for the microfluidics experiments. The solution for the growth channel was prepared by making an aqueous solution containing BaCl_2 (19.1 mM) and Na_2SiO_3 (82.0 mM) in deionized water through which N_2 gas was bubbled to remove CO_2 . The pH was then adjusted to either 11.9 or 11.2 using NaOH and HCl . The solution for the CO_2 channel contained 20 mM NaHCO_3 in deionized water. The pH was set to 7.0 using NaOH .

D) Experimental procedure and image analysis. Both the growth channel and CO_2 channel were flushed with degassed water at a rate of ca. $100 - 150 \mu\text{L}/\text{min}$ for approximately 15 min to remove CO_2 and air bubbles from the PDMS. The syringes containing the $\text{BaCl}_2/\text{Na}_2\text{SiO}_3$ and CO_2 solutions were connected to the tubings that lead to the growth channel and CO_2

channel, respectively (Fig. S1). To start the growth, the $\text{BaCl}_2/\text{Na}_2\text{SiO}_3$ solution was pumped at $100\mu\text{L}/\text{min}$ for 5 min and subsequently reduced to $8.15\mu\text{L}/\text{min}$. The precipitation of the structures was initiated by switching on the CO_2 flow ($50\mu\text{L}/\text{min}$) and the process was followed in real time using a Leica DMRX optical microscope equipped with polarizers (Fig. 1 G and Movie S1). Image analysis was performed with an in-house programmed MATLAB script that identified the formation of new structures and tracked their development as a function of time. This allowed us to measure the growth rates of nucleated sites from the time-lapse images that were taken using optical microscopy (Fig. 1 H).

E) Formation of periodic bands in the microfluidic chamber. The periodic formation of bands can be rationalized by a nucleation/precipitation/depletion mechanism reminiscent to so-called Liesegang bands. Starting from the membrane, the gradual flow of CO_2 into the growth channel induces the nucleation of a band of $\text{BaCO}_3/\text{SiO}_2$ coral-like structures. BaCO_3 crystallization favors growth on existing structures with exposed BaCO_3 sites rather than nucleating at a new site on the substrate. This initially confines growth to a single band. While the corals are growing, they locally deplete the solution and lower the pH over time. As the growth fronts of the neighboring structures approach each other, silica overcoating takes over and passivates the fronts at low pH. Only after this stage, new BaCO_3 nucleation events will take place, causing the formation of the next row of structures further away from the already grown ones. Overall, this process results in the formation of precipitation bands with spatial and temporal periodicity.

F) Model-guided sequential synthesis of functional shapes. In a 100 mL beaker, 0.210 g BaCl_2 and 0.048 g Na_2SiO_3 were dissolved in 45 mL degassed water. The solution was then transferred to a 50 mL syringe. A microfluidic tube was inserted through the spout of a 50 mL beaker containing a gold-coated glass slide, until it reached the bottom of the beaker. The other side of the microfluidic tube was connected to the 50 mL syringe containing the $\text{BaCl}_2/\text{Na}_2\text{SiO}_3$ solution. Using a syringe pump, 15 mL of the $\text{BaCl}_2/\text{Na}_2\text{SiO}_3$ solution was injected carefully in the beaker. Subsequently, this beaker was also covered with a petri dish lid. The pH in the vicinity of the growing structures was increased (decreased) by adding (subtracting) solution via the syringe. When CO_2 enters the beakers from the top, there is a vertical gradient in the CO_2 concentration and therefore also in the local pH, meaning that the highest pH is close to the bottom. By adding fresh $\text{BaCl}_2/\text{Na}_2\text{SiO}_3$ solution (0.3 mL in total, 1.0 mL/min), which has a high pH of 11.9, we raised the reacting solution from the bottom of the beaker, and thus increased the local pH around the growing structures on the glass slide. A similar effect can be induced by immersing a solid, such as a magnetic stirring bar, to the bottom of the beaker, which also causes the solution to rise, and thus locally increases the pH. Similarly, withdrawing the stirring bar from the solution decreases the local pH around the growing structures. When not coated by SiO_2 , the margins of the structures grown in a given regime serve as growth sites for a subsequent precipitation, and thus allow for the evolution of different architectures on top of each other. After ca. 180 min the glass slides were removed from the solution, washed twice

with water and then with acetone, and air-dried. Optical microscopy and SEM were used to analyze the structures that grew on the gold-coated glass slide (Fig. 4 A).

G) Synthesis of waveguiding microstructures with integrated light source. To grow the dyed seed crystals, 0.074 g BaCl_2 and 0.01 g Rhodamine B were dissolved in 15 mL of water in a 50 or 100 mL beaker. The pH of the solution was adjusted to $\text{pH} = 11.9$ using NaOH. A previously prepared gold-coated glass was vertically positioned in the solution and the beaker was covered with a petri dish. After ca. 45 min, the slide was removed from the solution, washed twice with water, subsequently washed with acetone and air-dried. For waveguiding helices (Fig. 4 C), 0.074 g BaCl_2 and 0.016 g Na_2SiO_3 were dissolved in 15 mL water and the pH was adjusted to 11.3 using HCl. The previously prepared glass slide was carefully positioned in the solution such that the BaCO_3 crystals were submersed. After ca. 1.5 – 2 hours the glass slide was removed from the solution, washed twice with water, subsequently washed with acetone and air-dried. To grow waveguiding trumpet shapes (Fig. 4 D), 0.084 g SrCl_2 and 0.016 g Na_2SiO_3 was dissolved in 15 mL water and the pH was adjusted to 11.9 using NaOH. The previously prepared glass slide was carefully positioned in the solution such that the BaCO_3 crystals were submersed. A petri dish was loosely placed on the beaker so that CO_2 from the air could enter the beaker. After ca. 75 min, the petri dish was carefully removed for 2 min to give a CO_2 pulse that resulted in the opening of the $\text{SrCO}_3/\text{SiO}_2$ stem shapes into vases (Fig. 4 B, sections in dark gray at the bottom, middle). Cleansing of the structures was performed as described above. Beamsplitting structures (Fig. 4 E) were prepared by dissolving 0.084 g SrCl_2 and 0.016 g Na_2SiO_3 in 15 mL water and adjusting the pH to 11.9 using NaOH. To induce the splitting of the growth front into an array of posts atop a coral-like structure (Fig. 4 B, sections in dark gray at the bottom, right), the temperature was lowered to 4°C for 15 min and subsequently increased to 40°C . Cleansing of the structures was performed as described above. Fluorescence microscopy with a Rhodamine filter and scanning electron microscopy were used to analyze the slides.

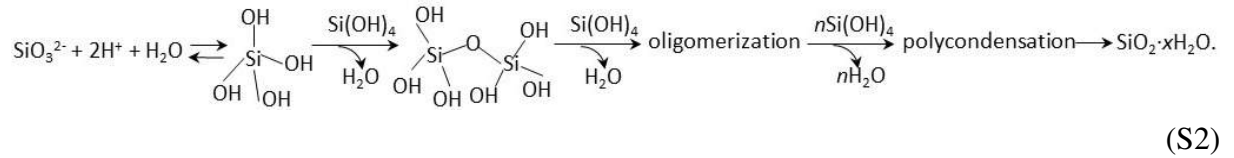
H) Transmission electron microscopy (TEM) procedure. TEM samples were prepared through two main techniques: direct growth on TEM copper grid and focused ion beam (FIB) milling. For direct growth samples, copper mesh TEM samples were attached on aluminum substrate during the synthesis and imaged with a TEM instrument subsequently (JEOL 2011 operated at 120 kV and JEOL 2010F operated at 200 kV). For FIB milling method, structures of interest were identified and transferred in situ with a micromanipulator (OMNIProbe) inside a Helios Nanolab 660 Dual Beam electron microscope (FEI, OR) before a protective layer was laid down on top of the structures ($\text{PT} \sim 1\mu\text{m}$). The specimens were then sequentially thinned by FIB at 30, 16, 5, and 2 kV ion beam voltages in order to reach electron transparency. TEM images with typical bright-field, dark-field, and SAED techniques were taken by using a JEOL 2011 operated at 120 kV. The image magnification and camera constants were calibrated using as standard sample (MAG*I*CAL, Electron Microscopy Sciences, PA). HRTEM imaging was carried out using a field emission JEOL 2010F at 200 kV.

II. Supplementary text

A) Carbonate-silica coprecipitation and emergence of thin walls. When the influx of CO_2 causes the nucleation of BaCO_3 crystals on the substrate, the pH decreases around the growing crystal through the simplified chemical reaction



In turn, the lowering of the local pH triggers the acid-catalyzed polycondensation of metasilicate ions and formation of silica polymers that deposit on the BaCO_3 crystal through the reaction:



The simplified form of Eq. S2 is $\text{SiO}_3^{2-} + 2\text{H}^+ \rightarrow \text{SiO}_2 + \text{H}_2\text{O}$. The anisotropy of BaCO_3 needles that are elongated in the c -axis direction, in which the growth rate is fastest, results in preferential silica precipitation and passivation of the slow-growing faces of BaCO_3 crystals whereas the faster-growing faces in the c -axis are less coated and continue growing through the coprecipitation reactions. The silica-induced growth inhibition orthogonal to the growth direction results in the formation of anisotropic BaCO_3 nanocrystals that are embedded in the SiO_2 scaffold. The soluble silica polymers buffer the local acidity and act as slow diffusing species in the solution. Importantly, if the silica deposition rate exceeds that of BaCO_3 even in the fastest growth direction, the growing fronts become fully passivated by the silica coat, leading to complete termination of coprecipitation. The incomplete, directional overcoating of carbonate by silica may only persist when the BaCO_3 growth rate is sufficiently high. Therefore successful carbonate-silica coprecipitation can only occur at the outskirts of the SiO_2 pH range where silica deposition rate is low (see Fig. 1 F in the main text), in order to sustain continuous carbonate precipitation. The described mechanism can be validated and visualized using a microfluidic reactor in which exact reaction conditions can be controlled (Section I. B-E), in particular by the dynamic modulation of the CO_2 concentration (Fig. S2). Slowing down the growth of BaCO_3 by lowering the CO_2 inflow in the microfluidic channel results in the overcoating of BaCO_3 crystals by silica at the growth front, entirely hampering the growth of BaCO_3 and in turn the co-precipitation (Fig. S2 A). After switching on the CO_2 flow again, new structures can grow from the active growth sites embedded deep inside the already grown structures (false-colored red in the SEM) instead of the continuation of coprecipitation at the growth sites of the original wall (false-colored green in the SEM) (Fig. S2 C). Once a microstructure is completely passivated by silica, any increase of the CO_2 concentration leads to new BaCO_3 nucleation elsewhere on the substrate (indicated by arrows) but not on the silica overcoated $\text{BaCO}_3/\text{SiO}_2$ structures (Fig. S2 B).

The crystallographic characteristics of the BaCO_3 phase within the Regime I and II microstructures were studied by transmission electron microscopy (TEM) and selected area elec-

tron diffraction (SAED) (Fig. S3, S4, see Sec. I. H for the TEM procedure). At the wall of a vase-like structure (Fig. S3 A-D), the SAED pattern (Fig. S3 E) reveals that the c -axis of BaCO_3 in witherite form (orthorhombic structure) is aligned with the growth direction. The high-magnification image of the wall also reveals that the long axes of the rod-like structures, are aligned with the local growth direction (Fig. S3 F).

In Regime II, the 2D helical structures grow and undergo curling under confinement in a thin film of the solution, and hence have a finite structure height (22) (Fig. S4 A, B). At a slice of the 2D helical structure (Fig. S4 A, B), multiple diffraction patterns were taken from SAED (Fig. S4 C-E) and indexed as BaCO_3 with witherite structure with zone axis of $[100]$. More importantly, the c -axes are aligned with the morphological direction of the helical rotation (Fig. S4 D, E), which indicates that the crystals are also aligned with the local growth direction. This observation is consistent with previous measurements on the $\text{BaCO}_3/\text{SiO}_2$ composite structures formed in silica gels (20). A similar co-alignment between the c -axis and growth direction was also observed in vase-like structures (Fig. S3). We conclude that in both regimes, rod-like carbonate nanocrystals show a preferential alignment of the c -axis with the growth direction.

The presence of a silica-dominated boundary layer was also evident by examining the structural organization across an inner boundary in the 2D helical structure through high-resolution transmission electron microscopy (HRTEM) (Fig. S4 F-H). From the boundary to the interior of the structure, the relative amount of the crystalline carbonate phase appears to increase gradually (from Fig. S4 G, H).

The relative deposition rates of BaCO_3 and SiO_2 directly control the wall thickness of the structures during growth. The local diffusion gradients of acid arising from coprecipitation induce a nonuniform distribution of the pH around the growth front (Fig. S5 A). Silica precipitation mainly occurs along the lateral boundaries defining the wall (gray boundaries in Fig. S6 B, insets), while BaCO_3 nanocrystals grow between the silica layers that bound the wall (red regions shown in Fig. S6 B, insets). The microscopic spatial distribution of BaCO_3 and SiO_2 can be visualized by selectively dissolving the BaCO_3 using 0.5M HCl, which removes the inner part of the walls that is mainly composed of BaCO_3 , leaving behind only the SiO_2 cladding that covers the sides of the structures (Fig. S5 B-D).

The relative amounts of the deposited BaCO_3 and SiO_2 are set by the mutual feedback mechanism. Electron Dispersive X-Ray spectroscopy study reveals the $\text{BaCO}_3/\text{SiO}_2$ ratio as $89\pm3\%/11\mp3\%$ in Regime I and $78\pm4\%/22\mp4\%$ in Regime II. The increase in the SiO_2 precipitation for a lower pH in Regime II is consistent with the relative solubilities and reaction rates of BaCO_3 and SiO_2 (22). These fixed values, in turn, result in a constant surface-to-volume ratio of the cross-sectional carbonate-rich area (A) to the silica-rich boundary (S) and restrict the wall thickness. For example, in coral-like architectures for all four configurations of the constituent structures – posts, walls, wall ends, and junctions (Fig. S6, Table S1), we found that $A/S \sim 0.25 - 0.4\mu\text{m}$, which sets the thickness of the walls to $2A/S \sim 0.5 - 0.8\mu\text{m}$. The walls continue to grow laterally to sizes on the scale of $10\mu\text{m}$ or larger, leading to very low aspect ratio systems.

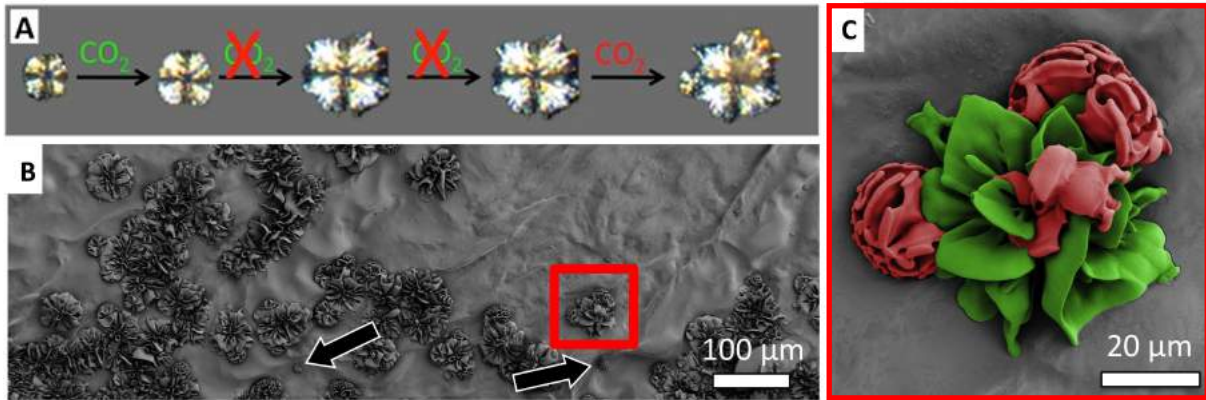


Fig. S2: Silica overcoating of the growing front and passivation of coprecipitation. (A) Optical polarized light microscopy images of a coral-like structure that initially grows when the CO_2 is first introduced. When the CO_2 input is stopped, the structures initially continue growing until some regions abruptly come to a halt as they become completely passivated by silica, resulting in a highly irregular morphology. As the CO_2 flow is subsequently switched on again, some regions of the structure resume growth. (B, C) Scanning electron microscopy (SEM) was used to investigate the same structure in more detail (the area inside the red box). (C) False-colored SEM image shows that, after switching on the CO_2 flow again, new structures (red) may grow from the active growth sites embedded deep inside the already grown structures (green). This demonstrates that the active growth sites of the original structure indeed became passivated. With hardly any active growth sites remaining, the secondary increase in the CO_2 concentration results in the nucleation of new structures next to the already formed ones, as indicated by the arrows in (B).

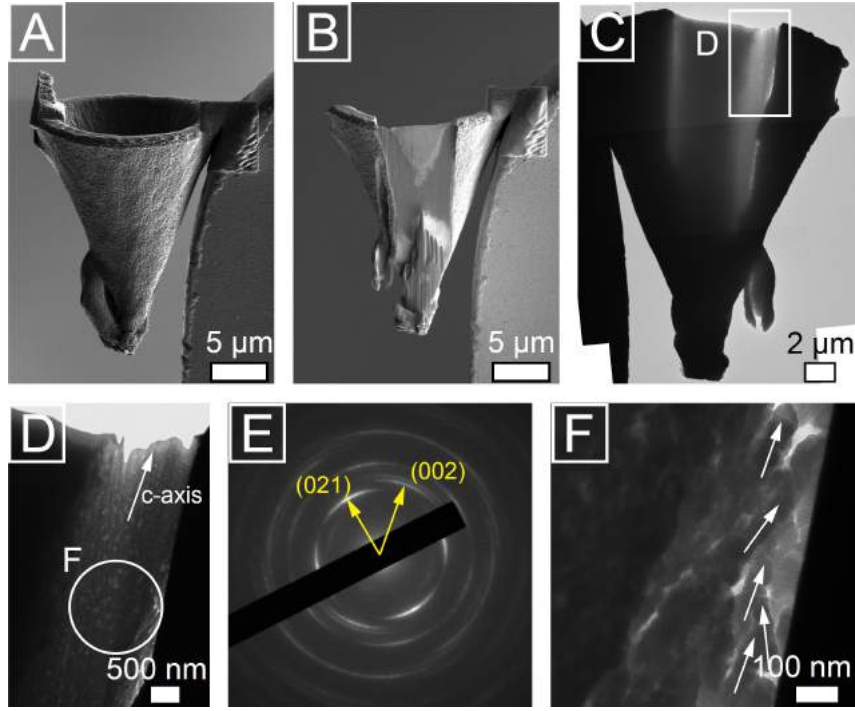


Fig. S3: **Fine structure of the precipitates from Regime I.** (A)-(D) An intact vase-like structure was picked up by an OMNIprobe, transferred to a copper TEM grid, and subsequently thinned down to become electron transparent. (E) A diffraction pattern taken from the SAED measurements at the wall of the vase. (F) The high-magnification image of the wall (shown in D) also reveals rod-like structures (aligned along white arrows).

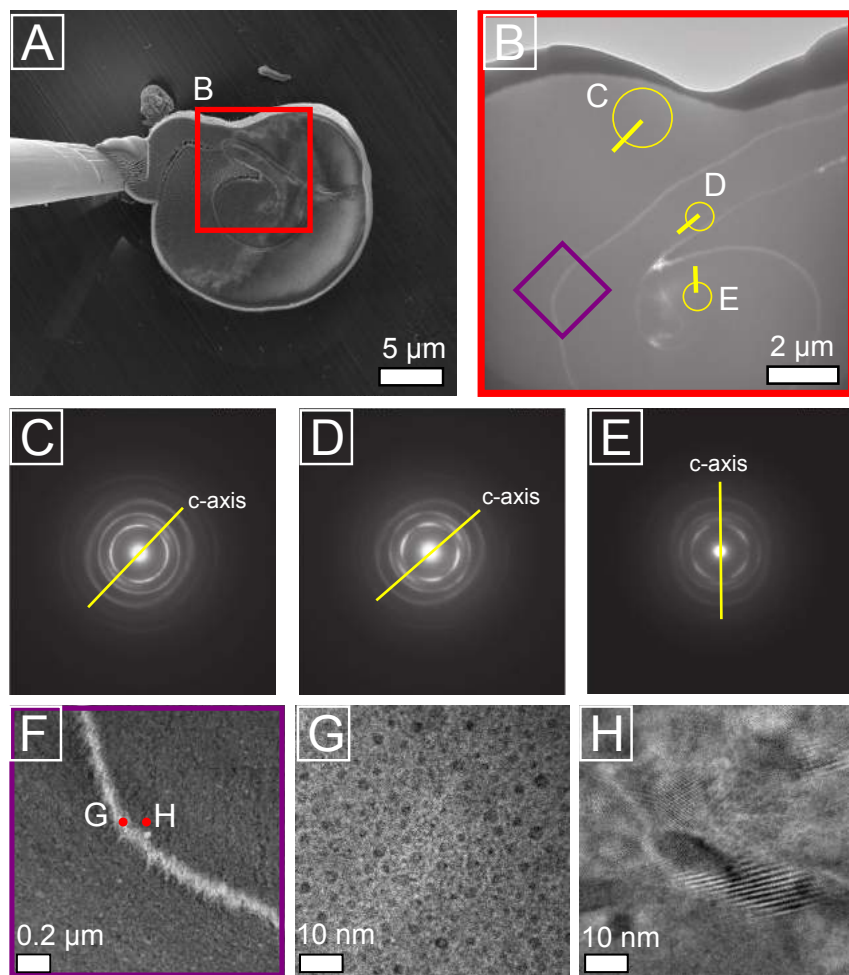


Fig. S4: **Fine structure of the precipitates from Regime II.** (A), (B) By using focused ion beam (FIB) milling, a horizontal TEM slice was prepared from a 2D curled precipitate, which forms in confinement in a thin film of the solution (22). Multiple SAED patterns were acquired at different locations of the structure, which are shown in (C)-(E) at higher magnification. (F) Multiple HRTEM images were taken across the thin boundary (the area surrounded by the magenta rectangle in B) at two different locations (G, H). It is seen that the structure changes from (G) merely an amorphous SiO_2 phase to (H) the coexistence of the BaCO_3 and amorphous SiO_2 . HRTEM analysis along the opposite direction yields an equivalent cross-over.

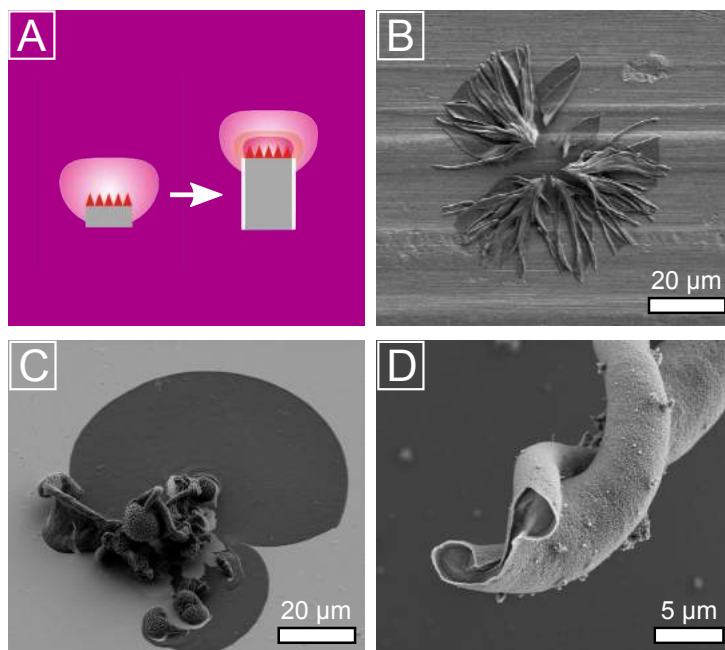


Fig. S5: **Wall composition of the microstructures (reproduced from Ref. (22)).** (A) Schematic of the cross-section of a growing wall and the nonuniform pH cloud atop it, where SiO₂ precipitates mainly at the wall sides (shown in white) and thereby fixes the wall thickness throughout growth. (B)-(D) Microstructures after selective dissolution of BaCO₃, revealing the SiO₂ scaffold that is covering the sides of the (B) coral-like and (C) helical structures. (D) Partial dissolution of BaCO₃ shows the SiO₂ layer while BaCO₃ crystals are still present deeper in the structure.

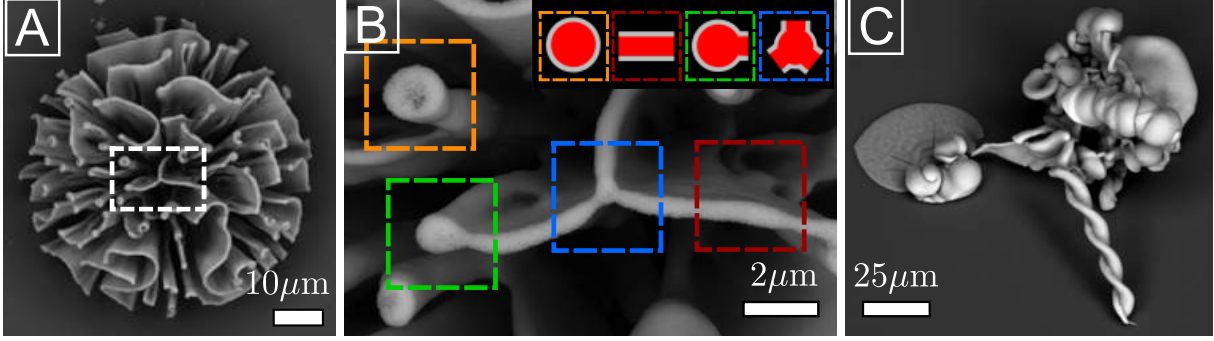


Fig. S6: **The growth of $\text{BaCO}_3/\text{SiO}_2$ microstructures.** (A) SEM image of a coral (Regime I). (B) In the enlarged view of the white-boxed region over the coral in (A), the ratio of the area of the growth front A to the boundary of the silica passivation S is calculated for each segment surrounded by the colored boxes. The cartoons of top view outline the simple two-dimensional geometries assumed for A (red) and S (gray) for each segment (Table S1). (C) A bundle of leaves, helices, and globular structures observed in Regime II.





| | Post | Wall | End of wall | Junction |
|----------------|---|---|---|---|
| |  |  |  |  |
| Area A | πr^2 | $I \times w$ | πr^2 | πr^2 |
| Boundary S | $2\pi r$ | $2I$ | $2\pi r - w$ | $2\pi r - 3w$ |
| Measurements | $r = 0.5\mu\text{m}$ | $w = 0.8\mu\text{m}$ | $r = 0.7\mu\text{m}, w = 0.4\mu\text{m}$ | $r = 0.4\mu\text{m}, w = 0.4\mu\text{m}$ |
| A/S | $0.25\mu\text{m}$ | $0.4\mu\text{m}$ | $0.4\mu\text{m}$ | $0.4\mu\text{m}$ |
| $w \sim 2 A/S$ | $0.5\mu\text{m}$ | $0.8\mu\text{m}$ | $0.8\mu\text{m}$ | $0.8\mu\text{m}$ |

Table S1: **Cross-sectional wall surface-to-area ratio.** Measurements of the cross-sectional carbonate-rich area (A) to the silica-rich boundary (S) ratio of the posts, walls, wall ends, and junctions in a coral (Fig. S6 A and B). These measurements yield the thickness (w) of the corresponding regions.

B) Equations of motion for the geometrical variables. Our theory models the dynamics of the curvilinear growth front in a fundamentally different way from that of conventional curves, such as vortex filaments in fluids (29, 30), where only the intrinsic geometry of the curve is relevant. This is because the configuration of the growth site is coupled with the extrinsic geometry of the embedding surface determined by its local orientation $\hat{\mathbf{N}}$, as well as the intrinsic geometries of the surface and the curve itself that are independent of $\hat{\mathbf{N}}$.

In Eq. 1, surface smoothness demands that the growth direction is tangential to the surface. This disallows a velocity component parallel to the local surface normal $\hat{\mathbf{N}}$, defined in Fig. S7.

Although a velocity component along the tangent of the curve $\partial\vec{\mathbf{X}}/\partial s$ (Fig. S7) may exist, we choose the growth direction $\hat{\mathbf{n}}$ to be orthogonal to both $\partial\vec{\mathbf{X}}/\partial s$ and $\hat{\mathbf{N}}$ in our model. This choice is associated with a gauge freedom for a closed curve with no loss of generality (27). For an open curve, however, the growth direction does not have to be orthogonal to $\partial\vec{\mathbf{X}}/\partial s$ at both ends of the curve; in that case our choice is a simplification. In this work, we confine ourselves to closed curves representing the growth front of precipitated morphologies. It is straightforward to generalize our framework to the motion of open curves leaving behind surfaces.

To calculate the set of equations governing the spatial and temporal dependence of the geometrical quantities, first we give their definitions (Table S2): Along the growth site, the geodesic curvature is given as $\kappa_g \equiv \hat{\mathbf{n}} \cdot \partial^2\vec{\mathbf{X}}/\partial s^2$, the normal curvature is $\kappa_N \equiv \hat{\mathbf{N}} \cdot \partial^2\vec{\mathbf{X}}/\partial s^2$, and the geodesic torsion $\tau_g \equiv \hat{\mathbf{N}} \cdot \partial\hat{\mathbf{n}}/\partial s$. On a curve perpendicular to the edge, the second normal curvature is given by $\kappa_{N,2} \equiv \hat{\mathbf{N}} \cdot d\hat{\mathbf{n}}/Udt$. The time derivative is defined in the frame comoving with the growth front, i.e. $d/dt \equiv \partial/\partial t|_{\vec{\mathbf{X}}(s,t)}$. Second, we note that $\hat{\mathbf{n}}$, $\hat{\mathbf{N}}$, and $\partial\vec{\mathbf{X}}/\partial s$ form an orthonormal set, so their scalar products are zero. Third, we define the infinitesimal arc length along the growth site as $ds \equiv \sqrt{g}d\sigma$. Here $g \equiv \partial\vec{\mathbf{X}}/\partial\sigma \cdot \partial\vec{\mathbf{X}}/\partial\sigma$ is the metric of the curve and σ is a fixed coordinate along the curve such that $\sigma \in [0, \sigma_{\max}]$ always (26).

One can arrive at the equations of motion of κ_g (Eq. S20), κ_N (Eq. S21), and τ_g (Eq. S23) by using (i) Eq. 1, (ii) the definitions of κ_g , κ_N , $\kappa_{N,2}$, and τ_g , as given in Table S2, (iii) the time evolution of the metric g (Eq. S6), (iv) a relation between mixed space and time derivatives at the curve (Eq. S7), and (v) the constraint that $\hat{\mathbf{n}}$, $\hat{\mathbf{N}}$, and $\partial\vec{\mathbf{X}}/\partial s$ form an orthonormal triad (Fig. S7). The three partial differential equations (PDEs) governing κ_g , κ_N , and τ_g impose mathematical constraints between the geometrical variables. Below, we will present the derivation of the PDEs in four steps.

1) Preliminary relations. In order to derive the equations that determine κ_g , κ_N , and τ_g , first we derive the preliminary mathematical relations. Since σ is time independent, the mixed partial derivatives satisfy the equality

$$\frac{\partial}{\partial\sigma} \frac{d}{dt} = \frac{d}{dt} \frac{\partial}{\partial\sigma}. \quad (\text{S3})$$

Next, we wish to obtain a relation between the mixed derivatives of the covariant derivative $\partial/\partial s$ and the time derivative. This requires determining the equation of motion of the metric g . Using Eq. S3, and taking the derivative of Eq. 1 with respect to σ and substituting the result in the time derivative of the metric yields

$$\frac{dg}{dt} = 2 \frac{\partial\vec{\mathbf{X}}}{\partial\sigma} \cdot \frac{\partial}{\partial\sigma} (\hat{\mathbf{n}}U). \quad (\text{S4})$$

Then, rewriting the spatial derivatives in terms of the covariant derivative, which satisfies $\sqrt{g}\partial/\partial s = \partial/\partial\sigma$, and the orthogonality relation $\hat{\mathbf{n}} \perp \partial\vec{\mathbf{X}}/\partial s$ transforms Eq. S4 into

$$\frac{dg}{dt} = 2gU \frac{\partial\vec{\mathbf{X}}}{\partial s} \cdot \frac{\partial\hat{\mathbf{n}}}{\partial s} = -2gU \frac{\partial^2\vec{\mathbf{X}}}{\partial s^2} \cdot \hat{\mathbf{n}}. \quad (\text{S5})$$

In Eq. S5 we have successively made use of the product rule $\vec{a} \cdot \vec{b}' = (\vec{a} \cdot \vec{b})' - \vec{a}' \cdot \vec{b}$, where \vec{a} and \vec{b} are vectors (accents denote derivatives), and $\hat{n} \perp \partial\vec{X}/\partial s$ to obtain the second equality. Substituting the definition of κ_g (Table S2), Eq. S5 becomes

$$\frac{d\sqrt{g}}{dt} = -\sqrt{g}\kappa_g U. \quad (\text{S6})$$

Eq. S6 governs the time dependence of the metric, in other words, the change of the local arc length during growth. Combining Eqs. S3, S6 and the relation $\sqrt{g}\partial/\partial s = \partial/\partial\sigma$ allows us to derive the following identity between the mixed derivatives,

$$\frac{d}{dt} \frac{\partial}{\partial s} = \frac{\partial}{\partial s} \frac{d}{dt} + \kappa_g U \frac{\partial}{\partial s}. \quad (\text{S7})$$

An equivalent expression was found for the curvature of a moving interface in two dimensions (27).

Obtaining the time variation of the geometrical variables involves evaluating the higher order derivatives of the unit vectors, as can be seen from the following example,

$$\frac{d\kappa_g}{dt} = \frac{d\hat{n}}{dt} \cdot \frac{\partial^2 \vec{X}}{\partial s^2} + \hat{n} \cdot \frac{d}{dt} \left(\frac{\partial^2 \vec{X}}{\partial s^2} \right). \quad (\text{S8})$$

Similarly, the right-hand sides of $d\kappa_N/dt$ and $d\tau_g/dt$ need to be calculated as well. In the following, we will evaluate these higher order derivatives by using Eq. 1, the definitions of κ_g , κ_N , τ_g , and $\kappa_{N,2}$, Eq. S7, the cross product $\hat{n} \times \hat{N} = \partial\vec{X}/\partial s$ and its cyclic permutations. Additionally,

$$\hat{a} \cdot \hat{a}' = 0 \quad (\text{S9})$$

always holds for any unit vector \hat{a} where prime denotes any derivative.

2) First-order derivatives. In the following, we evaluate the first-order space and time derivatives of the vectors \hat{n} , \hat{N} , and $\partial\vec{X}/\partial s$. Because of Eq. S9, $\partial^2 \vec{X}/\partial s^2$ does not have a component along $\partial\vec{X}/\partial s$, leading to the relation

$$\frac{\partial^2 \vec{X}}{\partial s^2} = \kappa_N \hat{N} + \kappa_g \hat{n}. \quad (\text{S10})$$

Next, we determine $\partial\hat{n}/\partial s$ by taking the derivative of $\hat{n} = \hat{N} \times \partial\vec{X}/\partial s$, which becomes

$$\frac{\partial\hat{n}}{\partial s} = \frac{\partial\hat{N}}{\partial s} \times \frac{\partial\vec{X}}{\partial s} - \kappa_g \frac{\partial\vec{X}}{\partial s}, \quad (\text{S11})$$

Since $\partial\hat{N}/\partial s$ should lie in the plane spanned by \hat{n} and $\partial\vec{X}/\partial s$, the first term of Eq. S11 on the right hand side must be either parallel or antiparallel to \hat{N} . Then, by using the definition of the geodesic torsion (Table S2), Eq. S11 becomes

$$\frac{\partial\hat{n}}{\partial s} = \tau_g \hat{N} - \kappa_g \frac{\partial\vec{X}}{\partial s}. \quad (\text{S12})$$

By virtue of the scalar product of $\hat{\mathbf{N}}$ with Eqs. S10 and S12, followed by using the product rule, the spatial derivative of $\hat{\mathbf{N}}$ is found as

$$\frac{\partial \hat{\mathbf{N}}}{\partial s} = -\tau_g \hat{\mathbf{n}} - \kappa_N \frac{\partial \vec{\mathbf{X}}}{\partial s}. \quad (\text{S13})$$

Now we calculate the time derivatives of the unit vectors. We start by evaluating $d(\partial \vec{\mathbf{X}}/\partial s)/dt$, which requires implementing Eq. S7, leading to

$$\frac{d}{dt} \frac{\partial \vec{\mathbf{X}}}{\partial s} = \frac{\partial}{\partial s} \frac{d \vec{\mathbf{X}}}{dt} + \kappa_g U \frac{\partial \vec{\mathbf{X}}}{\partial s}. \quad (\text{S14})$$

According to Eq. S9, $d(\partial \vec{\mathbf{X}}/\partial s)/dt$ must be orthogonal to the second term on the right hand side of Eq. S14. When $\partial(d \vec{\mathbf{X}}/dt)/\partial s$ is evaluated by using Eq. 1 and Eq. S12, then Eq. S14 becomes

$$\frac{d}{dt} \frac{\partial \vec{\mathbf{X}}}{\partial s} = U \tau_g \hat{\mathbf{N}} + \frac{\partial U}{\partial s} \hat{\mathbf{n}}. \quad (\text{S15})$$

The definition of the second normal curvature $\kappa_{N,2}$ (Table S2) allows us to determine the first component of $d\hat{\mathbf{n}}/dt$. Its second component can be extracted by dotting $\hat{\mathbf{n}}$ into Eq. S15 and using the product rule subsequently. These steps yield

$$\frac{d\hat{\mathbf{n}}}{dt} = U \kappa_{N,2} \hat{\mathbf{N}} - \frac{\partial U}{\partial s} \frac{\partial \vec{\mathbf{X}}}{\partial s}. \quad (\text{S16})$$

Taking the scalar product of $\hat{\mathbf{N}}$ with Eqs. S15 and S16 and applying the product rule gives $d\hat{\mathbf{N}}/dt$ as

$$\frac{d\hat{\mathbf{N}}}{dt} = -U \kappa_{N,2} \hat{\mathbf{n}} - U \tau_g \frac{\partial \vec{\mathbf{X}}}{\partial s}. \quad (\text{S17})$$

3) Higher-order derivatives. Next, we determine the expressions $d(\partial^2 \vec{\mathbf{X}}/\partial s^2)/dt$ and $d(\partial \hat{\mathbf{n}}/\partial s)/dt$, which are required to calculate $d\kappa_g/dt$ (Eq. S8), $d\kappa_N/dt$, and $d\tau_g/dt$. We start by applying Eq. S7 to $d(\partial^2 \vec{\mathbf{X}}/\partial s^2)/dt$, followed by taking the derivative $\partial/\partial s$ of Eq. S15, which corresponds to the first term from the preceding step. Then, using Eqs. S13, S12, and S10, respectively, in the resulting expression, we find

$$\begin{aligned} \frac{d}{dt} \left(\frac{\partial^2 \vec{\mathbf{X}}}{\partial s^2} \right) &= \hat{\mathbf{N}} \left[\frac{\partial}{\partial s} (U \tau_g) + \frac{\partial U}{\partial s} \tau_g + \kappa_g \kappa_N U \right] + \hat{\mathbf{n}} \left(-U \tau_g^2 + \frac{\partial^2 U}{\partial s^2} + \kappa_g^2 U \right) \\ &\quad - \frac{\partial \vec{\mathbf{X}}}{\partial s} \left(U \tau_g \kappa_N + \kappa_g \frac{\partial U}{\partial s} \right). \end{aligned} \quad (\text{S18})$$

Similarly, in order to evaluate $d(\partial\hat{\mathbf{n}}/\partial s)/dt$, we first apply Eq. S7 and then take the derivative $\partial/\partial s$ of the resulting first term (Eq. S16). After that, we use Eqs. S13, S10, and S12, respectively. These steps lead to

$$\begin{aligned} \frac{d}{dt} \left(\frac{\partial\hat{\mathbf{n}}}{\partial s} \right) &= \hat{\mathbf{N}} \left[\frac{\partial}{\partial s} (U\kappa_{N,2}) - \frac{\partial U}{\partial s} \kappa_N + \kappa_g \tau_g U \right] - \hat{\mathbf{n}} \left(U\tau_g \kappa_{N,2} + \kappa_g \frac{\partial U}{\partial s} \right) \\ &\quad - \frac{\partial \vec{\mathbf{X}}}{\partial s} \left(U\kappa_N \kappa_{N,2} + \frac{\partial^2 U}{\partial s^2} + \kappa_g^2 U \right). \end{aligned} \quad (\text{S19})$$

4) Geometrical compatibility relations. Evaluating Eq. S8 by making use of Eq. S10, Eq. S16, and Eq. S18, we arrive at

$$\frac{d\kappa_g}{dt} = \frac{\partial^2 U}{\partial s^2} + (\kappa_g^2 + \kappa_G) U. \quad (\text{S20})$$

This equation is in fact the differential form of the Gauss-Bonnet theorem, which relates the total Gaussian curvature of a surface $\kappa_G \equiv \kappa_N \kappa_{N,2} - \tau_g^2$ to the geodesic curvature of its boundaries (26). In that sense, the quantity $-\partial U/(U\partial s)$ is the geodesic curvature of the curve intersecting the growth site orthogonally.

To obtain $d\kappa_N/dt$, we substitute $\hat{\mathbf{n}}$ with $\hat{\mathbf{N}}$ in Eq. S8 and utilize Eqs. S10, S17, and S18. This yields

$$\frac{d\kappa_N}{dt} = \frac{\partial}{\partial s} (U\tau_g) + \tau_g \frac{\partial U}{\partial s} + \kappa_g (\kappa_N - \kappa_{N,2}) U. \quad (\text{S21})$$

Last, the equation of motion of the geodesic torsion is determined from

$$\frac{d\tau_g}{dt} = \frac{d\hat{\mathbf{N}}}{dt} \cdot \frac{\partial\hat{\mathbf{n}}}{\partial s} + \hat{\mathbf{N}} \cdot \frac{d}{dt} \left(\frac{\partial\hat{\mathbf{n}}}{\partial s} \right). \quad (\text{S22})$$

According to Eq. S22, adding the $\hat{\mathbf{N}}$ component of Eq. S19 to the scalar product of Eqs. S12 and S17 gives

$$\frac{d\tau_g}{dt} = \frac{\partial}{\partial s} (\kappa_{N,2} U) - \kappa_N \frac{\partial U}{\partial s} + 2\kappa_g \tau_g U. \quad (\text{S23})$$

Alternatively, by defining a second line element $ds^{(2)} \equiv U dt$ along a curve intersecting the growth site orthogonally, and noting that its geodesic curvature is given by $\kappa_g^{(2)} \equiv -\partial U/(U\partial s)$, the equations of motion of κ_g , κ_N , and τ_g can be derived from the partial differential equations of the surface theory, i.e. the Codazzi-Mainardi equations (26). Once the growth speed U is given by Eq. S26 as a series expansion in terms of the geometrical variables, we can then track the time evolution of the growth site, which constructs a surface in space and time, by solving Eqs. 2, S20, S21, S23, S26, and Eq. S6.

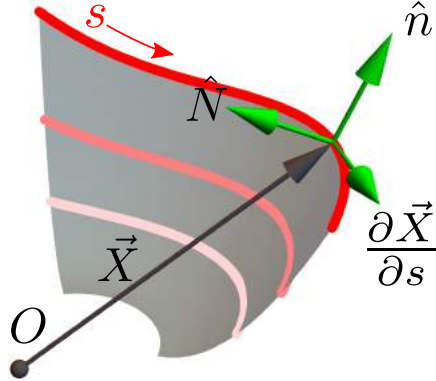


Fig. S7: **Growth of a surface.** (A) The growth front of a thin wall is represented in terms of a spatial curve with a position vector $\vec{X}(s, t)$, where s is the position along the curve. The tangent vector of the curve $\partial\vec{X}/\partial s$, the surface normal \hat{N} , and the growth direction \hat{n} form an orthonormal triad.

| Variable | Definition | Description |
|----------------|---|---|
| σ | $\in [0, \sigma_{max}]$ | fixed coordinate along the boundary curve |
| ds | $\sqrt{g}d\sigma$ | local arc length |
| g | $\partial\vec{X}/\partial\sigma \cdot \partial\vec{X}/\partial\sigma$ | metric of the boundary curve |
| κ_g | $\hat{n} \cdot \partial^2\vec{X}/\partial s^2$ | geodesic curvature |
| κ_N | $\hat{N} \cdot \partial^2\vec{X}/\partial s^2$ | normal curvature |
| τ_g | $\hat{N} \cdot \partial\hat{n}/\partial s$ | geodesic torsion |
| $\kappa_{N,2}$ | $\hat{N} \cdot d\hat{n}/Udt$ | 2nd normal curvature |

Table S2: **Definitions of the geometrical variables.**

C) Carbonate-silica coprecipitation versus regular solidification. We highlight the physical rationale behind our theoretical approach to the experimental measurements and previous works (20, 21, 22), based on the following outline: First, we clarify the differences between dendritic solidification and carbonate-silica coprecipitation. For the latter, the mechanism of bending at the interface, which gives rise to curled structures as a function of the solution pH, is explained in the main text. Using our observations of chemical precipitation reactions at the growth site, we quantify how growth via carbonate-silica coprecipitation can remain diffusion controlled yet strongly localized, distinct from the conventional solidification picture. This serves as a physical basis for our model of the growth rate as a function of interface geometry (Section II. D). The measurements in the microfluidic channel (Sections I. B–E) provide evidence for a diffusion-limited growth mechanism, as discussed in the main text. Furthermore, as noted in the main text, similar behavior was observed in an alkaline solution for a leaf where growth accelerates as the structure develops a tip (21).

Carbonate-silica coprecipitation produces solid structures in which carbonate in the crystalline state and silica in the amorphous state coexist. Therefore, growth through coprecipitation is fundamentally different than conventional growth of ionic crystals, both in terms of governing physico-chemical processes and the resulting thin-walled morphologies, which owe their complexity to the amorphous phase of polymerized silica as opposed to simpler shapes of carbonate crystals restricted by crystal symmetries. The carbonate crystal aggregation within the silica backbone thus plays a limited role in the development of form. This can be inferred from the difference between intricate geometries arising from $\text{BaCO}_3/\text{SiO}_2$ coprecipitation in Regimes I and II (defined in Fig. 1 F in the main text) and simple dendritic morphologies of BaCO_3 crystal precipitation when the original solution containing Na_2SiO_3 and BaCl_2 was set at pH below the silica deposition range (22). Here, the role of silica in pattern formation is likely analogous to protein-affected crystal growth, in that it shapes in situ the morphologies of the coprecipitating patterns.

In conventional solidification of bulk materials, the sole physical mechanism is the growth mode (either interface or diffusion controlled), which is determined by two length scales: The diffusion length L_D and the local radius of curvature L_H , where H is the mean curvature at a given point on the two-dimensional growth front. When $L_H \gg L_D$, growth must always be interface controlled as in spherulitic crystallization where growth reaches a steady state in an effectively one dimensional setting because the interface is nearly flat on length scales L_D . Conversely, when $L_H \ll L_D$, growth must be diffusion controlled since the curved front cannot reach a steady state (24).

Unlike conventional solidification/crystallization, thin-walled accretion of $\text{BaCO}_3/\text{SiO}_2$ coprecipitation involves two physical processes: tangential growth (Eq. S26) and bending (Eq. 2 in the main text). $\text{BaCO}_3/\text{SiO}_2$ coprecipitation is governed by three length scales (rather than two as in conventional solidification): The diffusion length L_D of the soluble oligomeric/polymeric species that are slowly diffusing nearby the growth front, the local radius of geodesic (in-plane) curvature L_{κ_g} of the one-dimensional growth front, and the wall thickness w that satisfies $w \ll L_{\kappa_g}$ because of the high aspect ratio of the wall ($w \sim 1\mu\text{m}$). The comparison among these three length scales sets the growth mode:

- (1) $L_D > L_{\kappa_g} \gg w$: growth is diffusion controlled,
- (2) $L_{\kappa_g} > L_D \gg w$: growth is diffusion controlled but more localized than (i). Growth does not reach a steady interface-controlled state as the diffusive flux will be effectively two dimensional, because $L_D \gg w$.
- (3) $L_{\kappa_g} \gg w \gg L_D$: growth is in steady state and thus interface controlled.

A comparison of the length scales L_{κ_g} , w , and L_D determines if/when coprecipitation results in diffusion-limited growth. When the growth rate increases with higher interfacial curvature, this means that growth is governed by a diffusive flux pointing outward (into the liquid phase) at the solid-liquid interface, as in a growing snowflake where the latent heat generated at the interface diffuses into the supercooled liquid (25). In our case the outward diffusive

flux is due to excessive silica polymer concentration at the interface, only partially permitted in the solid structure. The rest is rejected and has to diffuse away from the interface, setting the coprecipitation rate. Estimating $\sim 10^1 - 10^2$ monomers in a soluble oligomerized or polymerized silica chain brings the diffusion coefficient to $D \sim 10 - 100 \mu\text{m}^2/\text{s}$ at room temperature. Given that our system is an alkaline aqueous solution, the diffusion length is then $L_D \equiv D/\bar{U} \sim (10 \mu\text{m}^2/\text{s})/(1 \mu\text{m}/\text{min}) \sim 600 \mu\text{m}$ for silica polymers and $L_D \equiv D/\bar{U} \sim (100 \mu\text{m}^2/\text{s})/(1 \mu\text{m}/\text{min}) \sim 6 \times 10^3 \mu\text{m}$ for silica oligomers, where \bar{U} is the approximate speed of the front. The local radius of curvature at the interface is given by $L_{\kappa_g} = U_A/\bar{U} \sim 100 \mu\text{m}$, where $U_A \sim 50 \mu\text{m}^2/\text{min}$ is the areal growth rate extracted from the microfluidics measurements. Based on these estimates, we conclude that $L_D \geq L_{\kappa_g} \gg w$, which is at the interface of categories (1) and (2). Thus, growth must be diffusion limited in agreement with our microfluidics experiments (see main text and Sections I. B–E). Below we will show that our system falls into category (2) by defining an effective diffusion length $L_{D_{eff}}$ that takes into account the rate of localized coprecipitation reactions at the interface.

Another fundamental aspect of the growth mechanism is the chemical reactions happening at the interface, which localize the coprecipitation of crystalline BaCO_3 and amorphous SiO_2 into microstructures. To reveal the effect of the reaction rate and reactant concentration at the interface, we note that the modified Stefan condition in the presence of chemical reactions at the growth site is

$$\frac{-D}{\Delta c_0} \hat{\mathbf{n}} \cdot \vec{\nabla} c = \bar{U} \left[1 + \frac{\rho}{\Delta c_0} (c - c_s) \right]. \quad (\text{S24})$$

Here, c is the concentration of diffusing species controlling the growth rate, $\Delta c_0 \equiv c_L - c_S$ is the difference between equilibrium concentrations of the particles in the solid phase and the surrounding liquid phase. The dimensionless silica polymerization rate (assumed to be proportional to the production rate of SiO_2 due to precipitation reactions) is denoted by $\rho \equiv \tau_D/\tau_r$, where τ_D is the diffusion time scale and τ_r is the reaction time scale. When $\rho = 0$, the above equation reduces to the conventional Stefan condition for diffusion-limited growth. When the reactions are much faster than diffusion ($\tau_r \ll \tau_D$) leading to $\rho \gg 1$, furthermore $c - c_S$ and Δc_0 are at the same order, the modified Stefan condition reduces to

$$-D \hat{\mathbf{n}} \cdot \vec{\nabla} c = \rho \bar{U} (c - c_s). \quad (\text{S25})$$

Then, the effective diffusion length is given by $L_{D_{eff}} \equiv D/(\rho \bar{U})$, which is much smaller than the bare diffusion length L_D , i.e. $L_{D_{eff}} \ll L_D$. Clearly, the effect of localized chemical reactions can bring the relevant length scale to values smaller than the local radius of curvature $L_{\kappa_g} > L_{D_{eff}}$, constraining the relevant physical processes to the neighborhood of the growth front, still at bigger length scales than the wall thickness w ($L_{\kappa_g} > L_{D_{eff}} \gg w$). We conclude that within the classification above, the growth mode is in category (2), namely carbonate-silica coprecipitation is strongly localized as opposed to conventional solidification of bulk crystals, yet avoids a steady interface-controlled state owing to the thin-wall formation. Thus, a local growth model given by a power series expansion of the growth speed (Eq. S26) in terms of local geometric variables is a better approximation to diffusion-controlled growth in carbonate-silica

coprecipitation than in dendritic crystallization processes, which nevertheless was successfully applied and yielded an accurate qualitative description (27).

D) Determination of speed. We determine the local growth speed U by a power series expansion in terms of κ_g , its second derivative $\partial^2 \kappa_g / \partial s^2$, κ_N , τ_g , and $\kappa_{N,2}$. For reasons clarified below, we choose to truncate the expansion at the third order in an inverse characteristic length scale $1/\ell$, where ℓ sets the linear dimensions of the initial condition of the sculptures in the simulations. This approximation reproduces qualitatively the dynamics of the diffusion-limited precipitation, in analogy with the geometrical models of dendritic solidification (27). Furthermore, it simplifies the analysis because solving for diffusion fields around an evolving two dimensional structure in the space is cumbersome, and the boundary conditions modeling the constant wall thickness remain unknown.

In real units, the series expansion of the growth speed up to third order in $1/\ell$ is given by

$$U = -\alpha_1 \kappa_g + \alpha_2 \kappa_g^2 + \alpha_3 \kappa_g^3 + \eta_1 H^2 + \eta_{21} \kappa_N \kappa_{N,2} + \eta_{22} \tau_g^2 + \eta_3 \kappa_g H^2 - \eta_{41} \kappa_g \kappa_N \kappa_{N,2} + \eta_{42} \kappa_g \tau_g^2 + \eta_5 \tau_g H + \eta_6 \kappa_g \tau_g H - \lambda \frac{\partial^2 \kappa_g}{\partial s^2} + \mathcal{O}(\ell^{-4}), \quad (\text{S26})$$

where $H \equiv (\kappa_N + \kappa_{N,2})/2$ is the mean curvature of the surface, and the coefficients of each term are positive scalars. The term $\partial^2 \kappa_g / \partial s^2$ suppresses unstable outward kinks along the reaction front originating from the terms with κ_g , analogous to the Mullins-Sekerka instability in dendritic solidification (31). Therefore, the prefactor λ multiplying $\partial^2 \kappa_g / \partial s^2$ is proportional to the line tension along the growth front (27).

The power series given in Eq. S26 implies that growth may continue indefinitely albeit with an ever decreasing speed e.g. while a vase is precipitated, where only κ_g and κ_N are finite (Fig. S8 A and B). In Eq. S26, κ_g breaks the $\hat{n} \rightarrow -\hat{n}$ symmetry and is present at all orders, i.e. \hat{n} points to the solution whereas $-\hat{n}$ is directed to the solid. Additionally, there are no first order derivatives in the arc length coordinate s because U must remain unchanged under the transformation $s \rightarrow -s$. In contrast with the geodesic curvature κ_g , the extrinsic geometrical quantities κ_N , τ_g , and $\kappa_{N,2}$ appear as even terms since they change sign under $\hat{N} \rightarrow -\hat{N}$ transformation, under which U must remain invariant. In Eq. S26, these terms at order $\mathcal{O}(\ell^{-2})$ increase the growth speed when the associated deformations emerge. When the absolute values of any of κ_N , τ_g , and $\kappa_{N,2}$ become very large, then the terms penalizing the speed can enter the expansion first at the third order, namely by the product of any pair of these variables with κ_g . Thus, all of the third order terms in Eq. S26 are mainly responsible from decreasing the growth rate, including the terms proportional to κ_g^3 and $\partial^2 \kappa_g / \partial s^2$. Exceptions to these may occur when for instance $\eta_3 \kappa_g H^2$ reinforces the speed for $\kappa_g > 0$; however it is in general balanced by the other third order terms for a variety of sculptures simulated in this work. An expansion including the fourth order terms in $1/\ell$ would enable us to shift the speed penalty terms to this order, but such an expansion would produce many additional free parameters, making the numerical implementation and analysis tedious, without additional insight.

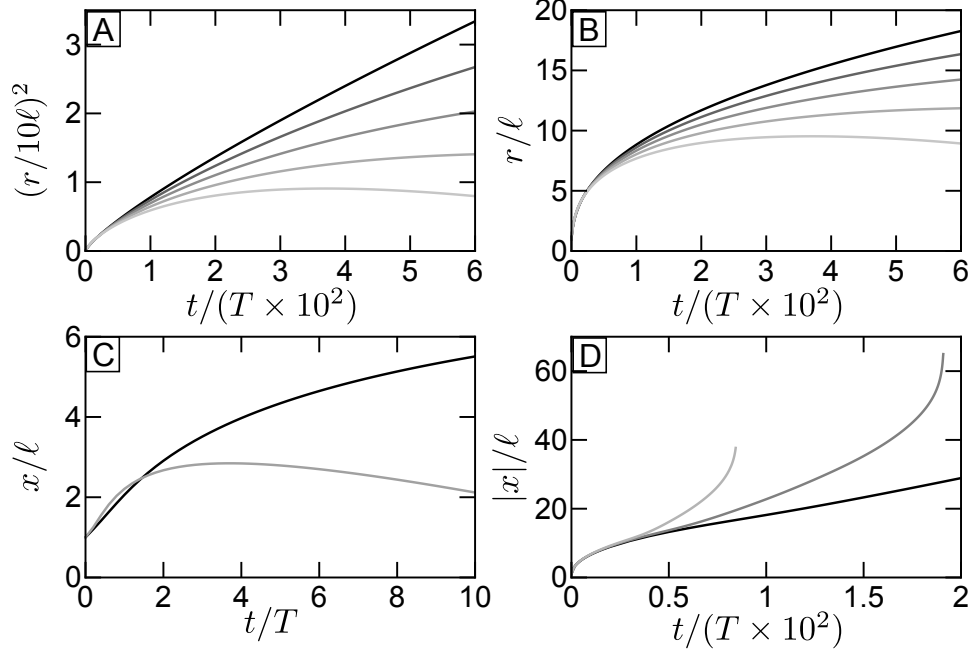


Fig. S8: Dynamics from the geometrical morphogenesis model. (A) The square of the radius, proportional to the projected area, and (B) the radius of the projected area enclosed by the circular growth site are shown as a function of time, giving rise to vases (Fig. 3 A). The grayscale changes from dark to light with the bending parameter increasing from $q_b = 10^{-3}$ to 0.013 in 3×10^{-3} increments. As a function of time, (C) demonstrates the position of the growth site of the petals along the x -axis ($y = 0$) for $q_b = 10^{-3}$ (black) and $q_b = 0.07$ (gray) (Fig. S9 B). (D) depicts the position of the growth site along the central axis of the helices ($y = 0, z = 0$) as a function of time for $q_b = 0.8, 0.9$, and 1 with the grayscale changing from dark to light, respectively (Fig. S10 from top to bottom).

E) Numerical implementation of the model and simulation parameters. Eqs. 2 and S26 incorporate the physical processes at work, whereas Eqs. S6, S20, S21, and S23 impose geometrical constraints along the growth site. These equations constitute our model, and we solve them by using the COMSOL 4.3a finite element package (<http://www.comsol.com>). Eqs. 2, S6, S20, S21, S23, and S26 form a set of coupled nonlinear partial differential equations, which is seventh order in space and first order in time. Thus, an initial condition for each of the variables and a total of seven boundary conditions at the two ends of the growth edge need to be determined. The growth starts either from a circle (vases, petals, structures grown in two and three steps) or a semicircle with small spatial perturbations (helices), where the initial direction of local growth \hat{n} is also determined for every sculpture. For structures with a circular margin at all times (vases or structures grown in two and three steps), the spatial dependence is irrelevant when the initial distribution of $\kappa_{N,2}$ is uniform and the line tension is sufficiently high so as to suppress any minute protrusions along the growth site ($\lambda \rightarrow \infty$). Then, the spatial derivatives

in Eqs. 2, S20, S21, S23, and S26 vanish, leading to an initial value problem. For petals and helices, the full boundary value problem is solved to account for spatial variations. Regardless of the structure under consideration, the fixed coordinate σ always increases in the clockwise direction since $\hat{\mathbf{n}}$, $\hat{\mathbf{N}}$, and $\partial\vec{\mathbf{X}}/\partial s$ form a right-handed coordinate system (Fig. S7). The initial and boundary conditions (in case there are any) are given as follows:

1) Vases or structures grown in two and three steps. The following surface vector parameterized by $\sigma \in [0, 1]$ along the interface and the height z constitutes the initial condition:

$$\vec{\mathbf{X}} = \{f(\epsilon, m, z, \sigma) \cos(2\pi\sigma), -f(\epsilon, m, z, \sigma) \sin(2\pi\sigma), z\}, \quad (\text{S27})$$

where $f(\epsilon, m, z, \sigma) \equiv 1 + mz + \epsilon \cos(2\pi\sigma)$. The angle of the slope β (Fig. 1 E) is equal to $\beta = 1/m$. For vases or structures grown in multiple steps, we set $\epsilon = 0$. The derivatives of Eq. S27 with respect to σ and z yield the vectors $\partial\vec{\mathbf{X}}/\partial\sigma$ and $\vec{\mathbf{n}} \equiv \sqrt{1 + m^2} \hat{\mathbf{n}}$. By using higher order derivatives and other relations from differential geometry (26), all geometric quantities are determined from Eq. S27 and evaluated at $z = 0$.

2) Petals. At $\sigma = 0$ (the intersection of the black lines with the initial circular configuration, see Fig. S9 B), $\partial\kappa_g/\partial s = \partial U/\partial s = \partial\kappa_{N,2}/\partial s = 0$, namely no-flux boundary conditions are implemented. Then $\tau_g = 0$ is trivially satisfied at $\sigma = 0$ as a fourth boundary condition (see Eq. S23) since the geodesic torsion of a planar circular interface is initially zero. At $\sigma = 1/2$, $\partial\kappa_g/\partial s = \partial\kappa_{N,2}/\partial s = 0$, and $U = 0$. The structures are symmetric with respect to a plane intersecting $\sigma = 0$, $\sigma = 1/2$, and extending along the z -direction. Again, Eq. S27 is used as an initial configuration of the front, where $\epsilon = 0$.

3) Helices. The initial condition is given by the following surface vector, which is parameterized by $\sigma \in [0, 1/2]$ along the interface and the radius r :

$$\vec{\mathbf{X}} = \left\{ -r \cos(2\pi\sigma), r \sin(2\pi\sigma), \delta \left[\frac{r}{R} \sin(2\pi\sigma) \right]^\xi \right\}, \quad (\text{S28})$$

where $R = 1$ in dimensionless units. The derivatives of Eq. S28 with respect to σ and r yield the tangent vectors of the surface $\partial\vec{\mathbf{X}}/\partial\sigma$ and $\partial\vec{\mathbf{X}}/\partial r$, respectively, which are not necessarily orthogonal to each other. The surface normal $\hat{\mathbf{N}}$ can be constructed by making $\partial\vec{\mathbf{X}}/\partial\sigma \times \partial\vec{\mathbf{X}}/\partial r$ a unit vector. Then, the initial condition of the growth direction can be determined from the relation $\hat{\mathbf{n}} = \hat{\mathbf{N}} \times \partial\vec{\mathbf{X}}/\partial s$. Both $\hat{\mathbf{n}}$ and $\hat{\mathbf{N}}$ are evaluated at $r = 1$, which correspond to a unit circular growth front decorated by a very small perturbation. Using the higher order derivatives and other relations from differential geometry (26) allows us to determine all geometric quantities from Eq. S28, which are again evaluated at $r = 1$. The initial growth orientation is nearly parallel to the plane of the semicircle to reproduce the effect of low nucleation densities in Regime II. The angle β defined in Fig. 1 E can be extracted as a function of σ from Eq. S28 and is very low.

The boundary conditions of the helix are; at $\sigma = 1/4$ (the point of the growth site restricted to $x = 0$ in Fig. S10), $\partial\kappa_g/\partial s = \partial U/\partial s = \partial\kappa_{N,2}/\partial s = 0$, namely no-flux boundary conditions are implemented. Then, $\tau_g = 0$ is trivially satisfied at $\sigma = 1/4$ as a fourth boundary condition since its initial value is zero (see Eq. S23). The remaining three boundary conditions are imposed at $\sigma = 0$ (the central axes at $y = 0$ and $z = 0$ in Fig. S10), which are $\partial\kappa_g/\partial s = \partial U/\partial s = 0$, and $\kappa_{N,2} = 0$.

We note that the geometrical constraints (Eqs. S6, S20, S21, and S23) are scale free. To define the dimensionless quantities of our model in terms of the physical parameters, first we give Eq. 2 in real units as

$$\frac{d\kappa_{N,2}}{dt} = D_1 \frac{\partial^2 \kappa_{N,2}}{\partial s^2} + \ell_1 \kappa_g \kappa_N U (\kappa_{N,2} - \bar{q}_b), \quad (\text{S29})$$

where D_1 is the diffusivity and ℓ_1 is the characteristic length scale of the geodesic curvature κ_g at which it affects the effective rate of folding. The dimensionless diffusivity in Eq. 2 is given as $\gamma \equiv D_1 T / \ell^2$, the folding rate is $\zeta \equiv \ell_1 / \ell$, and the dimensionless bending parameter is $q_b \equiv \bar{q}_b \ell$. Here T is the characteristic time scale, and ℓ is the radius of the initial circular configuration. The time scale is determined from the speed, and we choose it as $T \equiv \ell^2 / \alpha_1$. Eq. S26 stays the same when it is made dimensionless by defining $\bar{\alpha}_1 \equiv 1$, $\bar{\alpha}_2 \equiv \alpha_2 / \alpha_1 \ell$, $\bar{\alpha}_3 \equiv \alpha_3 / \alpha_1 \ell^2$, $\bar{\eta}_1 \equiv \eta_1 / \alpha_1 \ell$, $\bar{\eta}_{21} \equiv \eta_{21} / \alpha_1 \ell$, $\bar{\eta}_{22} \equiv \eta_{22} / \alpha_1 \ell$, $\bar{\eta}_3 \equiv \eta_3 / \alpha_1 \ell^2$, $\bar{\eta}_{41} \equiv \eta_{41} / \alpha_1 \ell^2$, $\bar{\eta}_{42} \equiv \eta_{42} / \alpha_1 \ell^2$, $\bar{\eta}_5 \equiv \eta_5 / \alpha_1 \ell$, $\bar{\eta}_6 \equiv \eta_6 / \alpha_1 \ell^2$, and $\bar{\lambda} \equiv \lambda / \alpha_1 \ell^2$, followed by dropping the bars of these definitions.

The speed of the curling rim propagating at the interface of a leaf, which later turns into a helix, was defined in Refs. (20, 21) as V_Φ . In our model, this speed determines the diffusivity of the $\kappa_{N,2}$ as $D_1 \equiv V_\Phi \ell$ (Eq. S29). In our simulations, we fix the dimensionless diffusivity as $\gamma \equiv D_1 T / \ell^2 = V_\Phi \ell / \alpha_1 = 2$. When $\ell \sim 2\mu\text{m}$, roughly twice the thickness of the walls, and the areal growth rate is taken as $\alpha_1 \sim 40\mu\text{m}^2/\text{min}$ (Eq. S33), we find the propagation speed of the bent region as $V_\Phi \approx 40\mu\text{m}/\text{min}$, which is at the same order of magnitude with $V_\Phi \approx 10\mu\text{m}/\text{min}$ as measured in Ref. (21). Additionally, the characteristic time scale of growth is found as $T \equiv \ell^2 / \alpha_1 \sim 0.1$ min.

The remaining simulation parameters for all calculations are as follows: $\zeta = 4$ for a right-handed coordinate system (see Fig. S7) and changes sign when switching to a left-handed coordinate system, i.e. ζ is a pseudoscalar. Furthermore, $\alpha_1 = 1$, $\alpha_2 = 5$, $\alpha_3 = 2$, $\eta_1 = \eta_{21} = 10$, $\eta_{22} = 5$, $\eta_3 = 20$, $\eta_{41} = 50$, $\eta_{42} = \eta_5 = \eta_6 = 0$, and $\lambda = 250$. Note that the coefficients associated with $\kappa_{N,2}$ are considerably bigger than α_1 , α_2 , and α_3 . This difference in the order of magnitude imposes rapid curling of the rim throughout the evolution of the helix, as observed in experiments. The structural variables present in the initial conditions are; for vases or structures grown in multiple steps $m = 0.5$ (Eq. S27); for petals $m = 0.5$, $\epsilon = 10^{-3}$ (Eq. S27); for helices $\delta = 2 \times 10^{-3}$ and $\xi = 7$ (Eq. S28).

The equations of motion of the geometrical variables, boundary conditions, and simulation parameters are listed in Table S3.

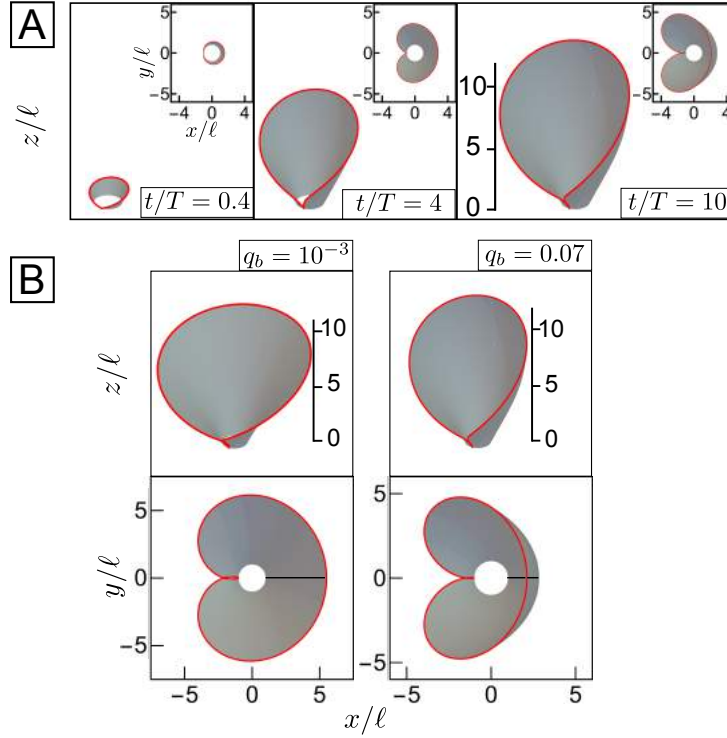


Fig. S9: **Calculated profiles of petals.** (A) The elevation and plan views demonstrate the time evolution of the petal growth for $q_b = 0.07$. The simulated petal growth at $q_b = 10^{-3}$ is shown in Fig. 3 B. (B) The copies of the petals from Fig. 3 B ($q_b = 10^{-3}$) and (A) ($q_b = 0.07$), which show the black ($\sigma = 0$) trajectories corresponding to the profiles of the time-dependent position of the growth site in Fig. S8 C. The fixed coordinate along the curve is denoted by σ . The red curves at each petal represent the growth sites. The lengths are scaled by ℓ , defined as the radius of a circular initial condition.

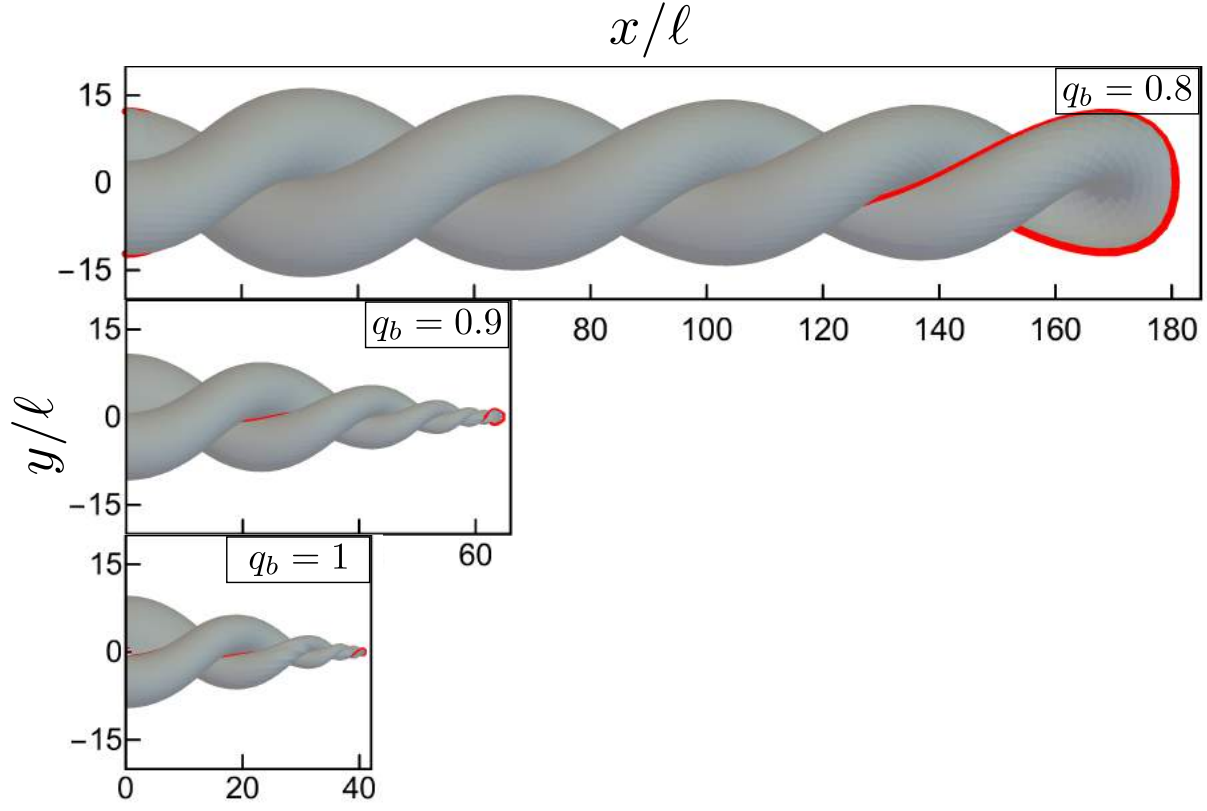


Fig. S10: **Calculated profiles of helices.** (A) Helices drawn to scale for $q_b = 0.8$, 0.9 , and 1 , from top to bottom. An exemplary growth process is shown in Fig. 3 C: At $q_b = 0.9$, a circular front lays down a section of a planar disk at early times (Fig. 3 C, $t/T = 20$). Simultaneously, minute initial height perturbations at one end of the front are amplified and give rise to local bending, as dictated by the source term in Eq. 2 when q_b is high. Due to the diffusion term in Eq. 2, the bend propagates along the advancing front until it reaches the apex with the boundary condition $\kappa_{N,2} = 0$ (Fig. 3 C, $t/T = 70$), which accounts for the symmetry between the oppositely curved regions. As the structure grows further at the apex (Fig. 3 C, $t/T = 100$), the front starts to twist around the central axis (Fig. 3 C, $t/T = 140 - 193$), leading to the double-helical structures that wind around each other. The red curves at each helix represent the growth sites. The lengths are scaled by ℓ , defined as the radius of a circular initial condition.

| Variable | Equation | |
|----------------|---|---------|
| κ_g | $\frac{d\kappa_g}{dt} = \frac{\partial^2 U}{\partial s^2} + (\kappa_g^2 + \kappa_G) U$, | Eq. S20 |
| κ_N | $\frac{d\kappa_N}{dt} = \frac{\partial}{\partial s}(U\tau_g) + \tau_g \frac{\partial U}{\partial s} + \kappa_g(\kappa_N - \kappa_{N,2})U$, | Eq. S21 |
| τ_g | $\frac{d\tau_g}{dt} = \frac{\partial}{\partial s}(\kappa_{N,2}U) - \kappa_N \frac{\partial U}{\partial s} + 2\kappa_g\tau_g U$, | Eq. S23 |
| $\kappa_{N,2}$ | $\frac{d\kappa_{N,2}}{dt} = \gamma \frac{\partial^2 \kappa_{N,2}}{\partial s^2} + \zeta \kappa_g \kappa_N U (\kappa_{N,2} - q_b)$, | Eq. 2 |
| g | $\frac{d\sqrt{g}}{dt} = -\sqrt{g}\kappa_g U$, | Eq. S6 |
| U | $U = -\alpha_1 \kappa_g + \alpha_2 \kappa_g^2 + \alpha_3 \kappa_g^3 + \eta_1 H^2 + \eta_{21} \kappa_N \kappa_{N,2} + \eta_{22} \tau_g^2 + \eta_3 \kappa_g H^2 - \eta_{41} \kappa_g \kappa_N \kappa_{N,2} + \eta_{42} \kappa_g \tau_g^2 + \eta_5 \tau_g H + \eta_6 \kappa_g \tau_g H - \lambda \frac{\partial^2 \kappa_g}{\partial s^2}$. | Eq. S26 |

| Structure | Position | Boundary condition |
|-----------|------------------|---|
| Petals | $\sigma = 0$, | $\partial \kappa_g / \partial s = \partial U / \partial s = \partial \kappa_{N,2} / \partial s = 0, \tau_g = 0^*$, |
| Petals | $\sigma = 1/2$, | $\partial \kappa_g / \partial s = \partial \kappa_{N,2} / \partial s = U = 0$, |
| Helices | $\sigma = 0$, | $\partial \kappa_g / \partial s = \partial U / \partial s = \kappa_{N,2} = 0$, |
| Helices | $\sigma = 1/4$, | $\partial \kappa_g / \partial s = \partial U / \partial s = \partial \kappa_{N,2} / \partial s = 0, \tau_g = 0^*$. |

| Equation | Parameters |
|----------|--|
| Eq. 2 | $\gamma = 2, \zeta = 4$ |
| Eq. S26 | $\alpha_1 = 1, \alpha_2 = 5, \alpha_3 = 2, \eta_1 = 10,$ $\eta_{21} = 10, \eta_{22} = 5, \eta_3 = 20, \eta_{41} = 50,$ $\eta_{42} = \eta_5 = \eta_6 = 0$, and $\lambda = 250$. |

Table S3: Equations of motion of the geometrical variables, boundary conditions, and simulation parameters. The partial differential equations governing the front motion, boundary conditions (see Sec.II. E 2 for petals and Sec.II. E 3 for helices), and variables. The boundary conditions denoted by * are trivially satisfied when other boundary conditions are specified as in the list (see Sec.II. E). The only parameter that is varied in the simulations is the bending parameter q_b . For the definitions of the parameters and initial conditions, see Sec.II. E.

F) Growth of the projected area of a vase and its limiting mechanism. In this section we intend to reveal the rate-limiting step of growth in Regime I, guided by the rate measurements in the microfluidics experiments. In a growing conical vase, only two of the curvatures, namely κ_g and κ_N are finite (Fig. 2 B). Furthermore, since the vase acquires a planar circular growth front, the spatial derivatives along the growth site vanish. Then, Eq. S20 at the interface of a conical vase, where the Gaussian curvature κ_G also vanishes, becomes

$$\frac{d\kappa_g}{dt} = \kappa_g^2 U. \quad (\text{S30})$$

When the growth rate is reaction or interface controlled, then the speed should be proportional to the reactant concentration C_x at the interface, namely $U \sim C_x$. It is well known

that the curvature of an interface alters the local concentration, such that it decreases if the interface protrudes into the solution and increases in a trough. This condition is known as the Gibbs-Thomson relation, and is given in our case as $C_x = C_0 + C_1 \ell \kappa_g$ (25). Here $C_0 > 0$ is the concentration at the wall front that is flat, and $C_1 > 0$ is the change in the concentration in response to the interface geometry, which is proportional to the line tension of the front. Furthermore, $\kappa_g < 0$ always throughout the evolution of a conical vase.

To reveal the limiting step of the growth, we will suppose the simplified general form for the speed

$$\tilde{U} \equiv \tilde{\alpha}_0 + \tilde{\alpha}_1 \kappa_g. \quad (\text{S31})$$

In case the growth is reaction limited, $\tilde{\alpha}_0$ and $\tilde{\alpha}_1 > 0$ are proportional to C_0 and C_1 , respectively. However, for a diffusion-limited growth mechanism as in Eq. S26, $\tilde{\alpha}_0 = 0$ and $\tilde{\alpha}_1 < 0$, i.e. the sign of $\tilde{\alpha}_1$ is such that it induces an instability due to the enhanced or suppressed diffusive flux of excess chemicals away from the curved interface. Then, Eq. S31 becomes a mere simplification of Eq. S26 at first order, where other higher order terms are zero.

Eqs. S30 and S31 permit a simple law for the areal growth rate. Defining the total curvature of a circular interface with a radius $r = r(t)$ as $\kappa \equiv 1/r$, and the angle between the vase wall and the substrate as β (Fig. 1 E), we find that the geodesic curvature is given by $\kappa_g = -\kappa \cos \beta$ and the normal curvature by $\kappa_N = \kappa \sin \beta$. Then, the combination of Eqs. S30 and S31, as well as the expression of the geodesic curvature in terms of the interface radius yield

$$\frac{1}{2} \frac{dr^2}{dt} = \tilde{\alpha}_0 r \cos \beta - \tilde{\alpha}_1 \cos^2 \beta. \quad (\text{S32})$$

Eq. S32 can also be recovered by replacing the normal curvature in terms of the total curvature into Eq. S21 and taking $\kappa_{N,2} = \tau_g = \partial U / \partial s = 0$. In order for the projected area to increase linearly in time as in the experiments, the right-hand side of Eq. S32 must be independent of the radius r and be positive. This means that $\tilde{\alpha}_0 = 0$ and $\tilde{\alpha}_1 < 0$, which indicates that the growth is controlled by diffusion. For Regime I, this result excludes the scenario unambiguously where the limiting factor is the reaction rates of BaCO_3 and SiO_2 , assuming that the projected area of the vases grows linear in time just like the corals in this regime.

Next, we determine $\alpha_1 > 0$ from the experiments, which is the scalar prefactor of the first term of the speed, as given in Eq. S26. When $\tilde{\alpha}_0 = 0$ and $\tilde{\alpha}_1 \equiv -\alpha_1$, Eq. S32 can be rewritten as

$$\frac{d(\pi r^2)}{dt} = 2\pi \alpha_1 \cos^2 \beta. \quad (\text{S33})$$

The right-hand side of Eq. S33 is equal to $30 - 50 \mu\text{m}^2/\text{min}$ in a microfluidic channel (Fig. 1 G, H). We find that $2\pi \cos^2 \beta \sim \mathcal{O}(1)$ for the values of the initial slopes used in the simulations, thus $\alpha_1 \sim 30 - 50 \mu\text{m}^2/\text{min}$.

III. Other supplementary materials

A) Stereolithography (STL) files

We provide STL files to enable the reader to 3D print the simulated sculptures or closely investigate their structural details in an STL file viewer, such as the freely distributed softwares Blender 2.76 (<https://www.blender.org/>) or MeshLab: an Open-Source Mesh Processing Tool (<http://meshlab.sourceforge.net/>). The URL link to the STL files in the Science database is given at the end of the main text. For printing purposes, thickness is added to the simulated surfaces via the “Solidify Modifier” option in Blender, and the modified structures are exported in the STL format. The ideal printing size of each sculpture is given in metric units in the file names along its longest cartesian dimension, in accordance with the coordinate system in the corresponding figure. Note that not all of the simulated structures in the STL files are to scale since e.g. the longest helix is roughly 18 times taller than a petal. Defining the scale of the vases as unity ($\tilde{s}_v \equiv 1$), the petals are at a scale $\tilde{s}_p = 3$, i.e. they are magnified three times with respect to a vase to highlight their details. The helix at $q_b = 0.8$ is at a scale $\tilde{s}_{h_1} = 0.75$, and the helices at $q_b = 0.9$ and $q_b = 1$ are at a scale $\tilde{s}_{h_2} = 1.25$. The scales of the structures grown in two and three steps are, respectively, $\tilde{s}_2 = \tilde{s}_3 = 1.5$.

B) Movies

Movie S1. The formation of coral-like structures in distinct bands inside a microfluidic chamber where the reaction conditions are controlled. CO_2 enters the channel via a semipermeable PDMS membrane that is situated at the bottom edge.

Movie S2. The simulated growth of two vase-shaped structures at the bending parameters $q_b = 10^{-3}$ and $q_b = 0.013$. Each second of the movie corresponds to $48T$, where T is the characteristic time scale of growth (see Section II. E for the definition of T). The red curves denote the growth site.

Movie S3. The simulated growth of two petal-shaped structures at $q_b = 10^{-3}$ and $q_b = 0.07$. Each second of the movie corresponds to $1.5T$. T is the characteristic time scale of growth (defined in Section II. E).

Movie S4. The simulated growth of a helix at $q_b = 0.8$. Each second of the movie corresponds to $96T$. T is the characteristic time scale of growth (defined in Section II. E).

Movie S5. The simulated growth of a helix at $q_b = 0.9$. Each second of the movie corresponds to $12T$. T is the characteristic time scale of growth (defined in Section II. E).

Movie S6. The simulated growth of a helix at $q_b = 1$. Each second of the movie corresponds to $6T$. T is the characteristic time scale of growth (defined in Section II. E).

Movie S7. The simulation of a two-step growth sequence. Each second of the movie corresponds to $12T$. The green curves denote the heights at which a change in q_b is imposed. T is the characteristic time scale of growth (defined in Section II. E).

Movie S8. The simulation of a three-step growth sequence. Each second of the movie corre-

sponds to $12T$. T is the characteristic time scale of growth (defined in Section II. E).

References

1. S. Xu, Z. Yan, K.-I. Jang, W. Huang, H. Fu, J. Kim, Z. Wei, M. Flavin, J. McCracken, R. Wang, A. Badea, Y. Liu, D. Xiao, G. Zhou, J. Lee, H. U. Chung, H. Cheng, W. Ren, A. Banks, X. Li, U. Paik, R. G. Nuzzo, Y. Huang, Y. Zhang, J. A. Rogers, Assembly of micro/nanomaterials into complex, three-dimensional architectures by compressive buckling. *Science* **347**, 154–159 (2015). doi:10.1126/science.1260960 [Medline](#)
2. P. X. Gao, Y. Ding, W. Mai, W. L. Hughes, C. Lao, Z. L. Wang, Conversion of zinc oxide nanobelts into superlattice-structured nanohelices. *Science* **309**, 1700–1704 (2005). doi:10.1126/science.1116495 [Medline](#)
3. B. M. Ross, L. Y. Wu, L. P. Lee, Omnidirectional 3D nanoplasmonic optical antenna array via soft-matter transformation. *Nano Lett.* **11**, 2590–2595 (2011). doi:10.1021/nl201516g [Medline](#)
4. M. Decker, M. W. Klein, M. Wegener, S. Linden, Circular dichroism of planar chiral magnetic metamaterials. *Opt. Lett.* **32**, 856–858 (2007). doi:10.1364/OL.32.000856 [Medline](#)
5. M. A. Kaliteevski, S. Brand, R. A. Abram, V. V. Nikolaev, Optical eigenmodes of a multilayered spherical microcavity. *J. Mod. Opt.* **48**, 1503–1516 (2001). doi:10.1080/09500340108231779
6. D. Brady, G. Papen, J. E. Sipe, Spherical distributed dielectric resonators. *J. Opt. Soc. Am. B* **10**, 644 (1993). doi:10.1364/JOSAB.10.000644
7. Y. Xu, W. Liang, A. Yariv, J. G. Fleming, S.-Y. Lin, Modal analysis of Bragg onion resonators. *Opt. Lett.* **29**, 424–426 (2004). doi:10.1364/OL.29.000424 [Medline](#)
8. J. H. Atwater, P. Spinelli, E. Kosten, J. Parsons, C. Van Lare, J. Van de Groep, J. Garcia de Abajo, A. Polman, H. A. Atwater, Microphotonic parabolic light directors fabricated by two-photon lithography. *Appl. Phys. Lett.* **99**, 151113 (2011). doi:10.1063/1.3648115
9. M. Munsch, N. S. Malik, E. Dupuy, A. Delga, J. Bleuse, J.-M. Gérard, J. Claudon, N. Gregersen, J. Mørk, Dielectric GaAs antenna ensuring an efficient broadband coupling between an InAs quantum dot and a Gaussian optical beam. *Phys. Rev. Lett.* **110**, 177402 (2013). doi:10.1103/PhysRevLett.110.177402 [Medline](#)
10. C. M. Soukoulis, S. Linden, M. Wegener, Physics. Negative refractive index at optical wavelengths. *Science* **315**, 47–49 (2007). doi:10.1126/science.1136481 [Medline](#)
11. J. K. Gansel, M. Thiel, M. S. Rill, M. Decker, K. Bade, V. Saile, G. von Freymann, S. Linden, M. Wegener, Gold helix photonic metamaterial as broadband circular polarizer. *Science* **325**, 1513–1515 (2009). doi:10.1126/science.1177031 [Medline](#)
12. J. L. Perry, K. P. Herlihy, M. E. Napier, J. M. Desimone, PRINT: A novel platform toward shape and size specific nanoparticle theranostics. *Acc. Chem. Res.* **44**, 990–998 (2011). doi:10.1021/ar2000315 [Medline](#)
13. J. R. Tumbleston, D. Shirvanyants, N. Ermoshkin, R. Januszewicz, A. R. Johnson, D. Kelly, K. Chen, R. Pinschmidt, J. P. Rolland, A. Ermoshkin, E. T. Samulski, J. M. DeSimone,

- Continuous liquid interface production of 3D objects. *Science* **347**, 1349–1352 (2015). doi:10.1126/science.aaa2397 [Medline](#)
14. S. S. Datta, A. Abbaspourrad, E. Amstad, J. Fan, S.-H. Kim, M. Romanowsky, H. C. Shum, B. Sun, A. S. Utada, M. Windbergs, S. Zhou, D. A. Weitz, 25th anniversary article: Double emulsion templated solid microcapsules: Mechanics and controlled release. *Adv. Mater.* **26**, 2205–2218 (2014). doi:10.1002/adma.201305119 [Medline](#)
 15. X. Ye, J. E. Collins, Y. Kang, J. Chen, D. T. N. Chen, A. G. Yodh, C. B. Murray, Morphologically controlled synthesis of colloidal upconversion nanophosphors and their shape-directed self-assembly. *Proc. Natl. Acad. Sci. U.S.A.* **107**, 22430–22435 (2010). doi:10.1073/pnas.1008958107 [Medline](#)
 16. L. A. Gower, D. A. Tirrell, Calcium carbonate films and helices grown in solutions of poly(aspartate). *J. Cryst. Growth* **191**, 153–160 (1998). doi:10.1016/S0022-0248(98)00002-5
 17. A. G. Shtukenberg, Y. O. Punin, A. Gujral, B. Kahr, Growth actuated bending and twisting of single crystals. *Angew. Chem. Int. Ed. Engl.* **53**, 672–699 (2014). doi:10.1002/anie.201301223 [Medline](#)
 18. Y.-Y. Kim, J. D. Carloni, B. Demarchi, D. Sparks, D. G. Reid, M. E. Kunitake, C. C. Tang, M. J. Duer, C. L. Freeman, B. Pokroy, K. Penkman, J. H. Harding, L. A. Estroff, S. P. Baker, F. C. Meldrum, Tuning hardness in calcite by incorporation of amino acids. *Nat. Mater.* **15**, 903–910 (2016). doi:10.1038/nmat4631 [Medline](#)
 19. J. M. García-Ruiz, S. T. Hyde, A. M. Carnerup, A. G. Christy, M. J. Van Kranendonk, N. J. Welham, Self-assembled silica-carbonate structures and detection of ancient microfossils. *Science* **302**, 1194–1197 (2003). doi:10.1126/science.1090163 [Medline](#)
 20. J. M. García-Ruiz, E. Melero-García, S. T. Hyde, Morphogenesis of self-assembled nanocrystalline materials of barium carbonate and silica. *Science* **323**, 362–365 (2009). doi:10.1126/science.1165349 [Medline](#)
 21. M. Kellermeier, E. Melero-García, F. Glaab, J. Eiblmeier, L. Kienle, R. Rachel, W. Kunz, J. M. García-Ruiz, Growth behavior and kinetics of self-assembled silica-carbonate biomorphs. *Chemistry* **18**, 2272–2282 (2012). doi:10.1002/chem.201102407 [Medline](#)
 22. W. L. Noorduin, A. Grinthal, L. Mahadevan, J. Aizenberg, Rationally designed complex, hierarchical microarchitectures. *Science* **340**, 832–837 (2013). doi:10.1126/science.1234621 [Medline](#)
 23. D. J. Belton, O. Deschaume, C. C. Perry, An overview of the fundamentals of the chemistry of silica with relevance to biosilicification and technological advances. *FEBS J.* **279**, 1710–1720 (2012). doi:10.1111/j.1742-4658.2012.08531.x [Medline](#)
 24. N. Goldenfeld, Theory of spherulitic crystallization. *J. Cryst. Growth* **84**, 601–608 (1987). doi:10.1016/0022-0248(87)90051-0
 25. J. S. Langer, Instabilities and pattern formation in crystal growth. *Rev. Mod. Phys.* **52**, 1–28 (1980). doi:10.1103/RevModPhys.52.1
 26. J. J. Stoker, *Differential Geometry* (Wiley, New York, 1969).

27. R. C. Brower, D. A. Kessler, J. Koplik, H. Levine, Geometrical approach to moving-interface dynamics. *Phys. Rev. Lett.* **51**, 1111–1114 (1983). [doi:10.1103/PhysRevLett.51.1111](https://doi.org/10.1103/PhysRevLett.51.1111)
28. B. Kahr, R. W. Gurney, Dyeing crystals. *Chem. Rev.* **101**, 893–951 (2001). [doi:10.1021/cr980088n](https://doi.org/10.1021/cr980088n) [Medline](#)
29. K. Nakayama, H. Segur, M. Wadati, Integrability and the motion of curves. *Phys. Rev. Lett.* **69**, 2603–2606 (1992). [doi:10.1103/PhysRevLett.69.2603](https://doi.org/10.1103/PhysRevLett.69.2603) [Medline](#)
30. H. Hasimoto, A soliton on a vortex filament. *J. Fluid Mech.* **51**, 477 (1972). [doi:10.1017/S0022112072002307](https://doi.org/10.1017/S0022112072002307)
31. W. W. Mullins, R. F. Sekerka, Stability of a planar interface during solidification of a dilute binary alloy. *J. Appl. Phys.* **35**, 444–451 (1964). [doi:10.1063/1.1713333](https://doi.org/10.1063/1.1713333)